SPOT PATTERNS OF THE SCHNAKENBERG REACTION-DIFFUSION SYSTEM ON A CURVED TORUS

J. C. TZOU*, L. TZOU†

ABSTRACT. For the Schnakenberg activator-inhibitor model on a torus, in the singularly perturbed regime of small activator to inhibitor diffusivity ratio $\varepsilon^2 \ll 1$, we derive a reduced ODE describing the influence of curvature on the the slow drift dynamics of a single localised spot, and also stability thresholds to fast amplitude instabilities of one- and two-spot patterns. By way of a hybrid asymptotic-numerical analysis, we obtain the results in terms of certain quantities associated with the Green's function for both the Laplace-Beltrami (Δ_g) and Helmholtz ($\Delta_g - V$) operators on the torus. To this end, we introduce a new analytic-numerical method for computing Green's functions on surfaces that requires only the numerical solution of a problem that is as regular as is desired. This allows properties of Green's functions at the location of the singularity to be determined to a high degree of accuracy. The method is applicable to operators of the form $\Delta_g + X - V$ for any metric tensor g, first order differential operator X, and smooth potential V. It centers on a microlocal approach for analytically determining the coefficients of all singular terms of the local behavior of a Green's function inside a region around the singular point. Remaining terms of the Green's function are solved for numerically using finite differences. The primary purpose of this paper is to both introduce the theoretical underpinnings of this technique and to numerically demonstrate its ability to accurately yield properties of a Green's function on a curved surface. All results are confirmed by numerical finite element solutions of the Schnakenberg reaction-diffusion system on the torus.

Keywords: reaction-diffusion system, localized spot patterns, Green's functions on curved surfaces, microlocal analysis, Hadamard parametrix

1. INTRODUCTION

Since the pioneering study of Pearson [27] in 1993 numerically demonstrating complex spatio-temporal dynamics of large amplitude, localized patterns of the 2-dimensional Gray-Scott activator-inhibitor reaction-diffusion system, there has been an intense focus in the analysis of such solutions. Of particular interest has been localized spot patterns in singularly perturbed activator-inhibitor reaction-diffusion systems [31], where the diffusivity $\varepsilon^2 \ll 1$ of the activator is asymptotically small compared to that of the $\mathcal{O}(1)$ diffusivity of the inhibitor. In this limit, spot solutions exist in which the activator is concentrated within an $\mathcal{O}(\varepsilon)$ region around N well-separated discrete points in the domain, and is asymptotically small otherwise (see, e.g., Fig. 2 of [27] and Fig. 1 of [20]). The spots interact via the inhibitor, which varies over an $\mathcal{O}(1)$ spatial scale globally over the domain.

Such solutions to singularly perturbed reaction-diffusion systems were first constructed, and their dynamics and stability analytically determined, in the 1-D setting using matched asymptotic methods [10, 16, 19]. Using a hybrid asymptotic-numerical method pioneered by Ward et al. in 1993 [46], the 2-D problem was solved by Kolokolnikov et al. in 2009 [20] for the Schnakenberg model on the unit disk and rectangle. The asymptotic results for the stability and dynamics of N-spot solutions relied on detailed knowledge of a certain Green's function at the location of the singularity. This Green's function encodes information regarding the geometry of the domain, as well as pairwise interactions between the spots.

Date: Mar. 12, 2019.

*Department of Mathematics and Statistics, Macquarie University, Sydney, NSW, Australia justin.tzou@mq.edu.au.

†School of Mathematics and Statistics, University of Sydney, Sydney, NSW, Australia leo.tzou@gmail.com.

Funding: The second author was supported by grants ARC DP190103451 and ARC DP190103302.

The hybrid method was adapted to obtain stability [32] and dynamics [39] results for spot patterns on the surface of the sphere in 2014 and 2016, respectively. In [39], detailed results for the existence and bifurcation structure of N-spot solutions were also obtained. In 2017, the method was extended to obtain analogous results for spot patterns in the 3-D interior of the unit ball [42].

In all of the above geometries, i.e., the disk, square, rectangle, surface of the sphere, and the interior of the ball, it is often possible to obtain certain Green's functions, such as the source-neutral Green's function, in either closed form or via a series solution. In geometries where this is not possible, one may still obtain an accurate Green's function by first removing from it the analytically known free space Green's function, then solving numerically for the smooth remainder. The accuracy of this approach was demonstrated in [24], where it was combined with a hybrid asymptotic-numerical method for obtaining the full distribution of capture times of a random particle by small targets inside a flat 2-D domain.

This approach relies upon the ability to analytically obtain the free space Green's function. However, when the underlying geometry is some variably curved surface with metric tensor g, and the operator for which the Green's function is sought takes the form $\Delta_g + X - V$, where X is some first order differential operator, and V is some smooth potential, the analogous free space Green's function is often not known. In analyses that require the gradient of the differentiable part of the Green's function at the location of the singularity, or even worse, the Hessian of the twice differentiable part, another method must be sought for accurately removing the singular terms of the desired Green's function in order to obtain a smooth numerical problem for the remainder.

The study of dynamics and stability of patterns on variably curved surfaces becomes relevant in the study of vegetation patterns that form in semi-arid environments. It has been shown [1, 26, 28] that the curvature of the underlying terrain plays an important role in the movement and distribution of the patterns. Indeed, even in the assumption of a completely flat domain, it has been shown [34, 33, 18] that a sufficiently steep slope can stabilize a localized vegetation stripe and prevent it from breaking up into spots (see [18]). Building an analytic framework to model and account for the topography of the terrain is thus of vital importance. Toward this end, we introduce an analytic-numerical framework for accurately computing highly sensitive properties of Green's functions on a variably curved surface, which can then be used in concert with the above-mentioned hybrid asymptotic-numerical method in order to obtain detailed results on how curvature impacts the stability and dynamics of patterns. In particular, the method utilizes a microlocal approach to analytically remove singular terms of a Green's function, leaving a more "regular" problem for the remaining smooth term to be solved for numerically.

While this framework can be applied to a variety of reaction-diffusion systems and surfaces, we will consider the simple case of the Schnakenberg system on the surface of a ring torus embedded in three dimensions parametrized as

$$\begin{aligned} \mathbf{x} \equiv (x,y,z) = ((R + r\cos\theta_1)\cos\theta_2, (R + r\cos\theta_1)\sin\theta_2, r\sin\theta_1)\,; \\ \theta_1 \in [-\pi/2, 3\pi/2)\ , \quad \theta_2 \in [0, 2\pi)\ , \end{aligned} \tag{1.1a}$$

with the Jacobian determinant

$$J(\theta_1,\theta_2) \equiv r(R + r\cos\theta_1)\,, \tag{1.1b}$$

where the constants R and r denote the major and minor radii of the torus, respectively. In coordinate free expression, the Schnakenberg system for the activator v and inhibitor u can be written as

$$\tau\partial_t u = \Delta_g u + A - \frac{uv^2}{\varepsilon^2}\,, \qquad \partial_t v = \varepsilon^2\Delta_g v - v + uv^2\,; \qquad t > 0\,, \tag{1.2a}$$

where $0 < \varepsilon \ll 1$, g is the pullback of the Euclidean metric onto the torus with major and minor radii R and r respectively. For simplicity, we have taken the diffusivity of the inhibitor u to be unity. Along with the $\mathcal{O}(\varepsilon^{-2})$ coefficient on the nonlinear reaction term in the first equation, the $\mathcal{O}(1)$ diffusivity of u leads to a "tightly-coupled" inner core problem (see Eq. (3.4)). This is in contrast to the weak-coupling regime considered in [40], in which the diffusivity of the inhibitor was $\mathcal{O}(\varepsilon^{-2})$. While we study localized, large amplitude solutions to (1.2a) in the singularly perturbed $0 < \varepsilon \ll 1$ regime, the bifurcation structure of small amplitude patterns near onset have been studied for (1.2a) on the torus using pde2path [44].

In coordinates given by $\boldsymbol{\theta} \equiv (\theta^1, \theta^2)$, the metric g takes on the form

$$g_{jk} d\theta^j d\theta^k = r^2 d\theta^1 d\theta^1 + (R + r\cos\theta_1)^2 d\theta^2 d\theta^2 \,, \tag{1.2b}$$

and Δ_g, the Laplace-Beltrami operator with respect to the metric tensor g, is given by

$$\Delta_g \equiv -(R + r\cos\theta_1)^{-1} r^{-2} \partial_{\theta_1} (R + r\cos\theta_1) \partial_{\theta_1} - (R + r\cos\theta_1)^{-2} \partial^2_{\theta_2} \,. \tag{1.2c}$$

Note that we are using the "geometer's Laplacian" which has non-negative eigenvalues, and we have used superscript indices for θ_1 and θ_2 to facilitate the summation notation. In §3, in the limit of small $\mathcal{O}(\varepsilon)$, we construct an N-spot quasi-equilibrium solution to (1.2), characterized by solutions to (1.2) for which $v \sim 0$ everywhere on the surface of the torus except for N localized regions of $\mathcal{O}(\varepsilon)$ extent centered about discrete points $\mathbf{x}_1, \ldots, \mathbf{x}_N$ in which $v \sim \mathcal{O}(1)$. Interactions between the spots are mediated through the inhibitor component u, which varies smoothly over an $\mathcal{O}(1)$ spatial scale.

We adopt the hybrid asymptotic-numerical method of e.g., [39, 32, 8, 20, 42] to formulate the N-spot solution in terms of the unique source-neutral Green's function $G_N(\boldsymbol{\theta}; \boldsymbol{\theta}_0)$ satisfying

$$\Delta_g G_N = \frac{1}{|\Omega|} - \delta(\boldsymbol{\theta}; \boldsymbol{\theta}_0) \,; \qquad \int_\Omega G_N d\Omega = 0 \,, \tag{1.3a}$$

where Ω is the surface of the torus, $|\Omega|$ its surface area, $\boldsymbol{\theta} = (\theta_1, \theta_2)$ the coordinates, $\boldsymbol{\theta}_0 = (\theta_1^0, \theta_2^0)$ the location of the singularity, and

$$\delta(\boldsymbol{\theta}; \boldsymbol{\theta}_0) \equiv \frac{1}{J(\boldsymbol{\theta}_0)} \delta(\theta_1 - \theta_1^0) \delta(\theta_2 - \theta_2^0) \,, \tag{1.3b}$$

with $J(\theta)$ the Jacobian determinant defined in (1.1b) and $\delta(x)$ the usual one-dimensional Dirac delta function.

In §4, we formulate a system of differential algebraic equations (DAEs) that describe the slow $\mathcal{O}(\varepsilon^2)$ time-scale drift of an N-spot pattern. The leading order contributions to motion are mutually repulsive pairwise spot-spot interactions terms and self-interaction terms captured, respectively, by $\tilde{\nabla}_j G_N(\boldsymbol{\theta}_j; \boldsymbol{\theta}_i)$, $j \neq i$, where $\boldsymbol{\theta}_k$ is the location of the k-th spot, and $\tilde{\nabla}_j R_N(\boldsymbol{\theta}_j; \boldsymbol{\theta}_j)$, where $R_N(\boldsymbol{\theta}; \boldsymbol{\theta}_j)$ is the regular part of the source-neutral Green's function defined as

$$G_N(\boldsymbol{\theta}; \boldsymbol{\theta}_j) \sim -\frac{1}{2\pi} \log |\mathbf{x} - \mathbf{x}_j|_g + R_N(\boldsymbol{\theta}; \boldsymbol{\theta}_j) \;\text{ as }\; \boldsymbol{\theta} \to \boldsymbol{\theta}_j \,. \tag{1.4}$$

As a by-product of our construction we will (re)prove in Proposition 2.1 the classical fact that G_N has this expansion. The regular part $R_N(\boldsymbol{\theta}; \boldsymbol{\theta}_j)$ is finite and at least once differentiable at $\boldsymbol{\theta} = \boldsymbol{\theta}_j$. In (1.4), we denote $\tilde{\nabla} f(\boldsymbol{\theta}_i; \boldsymbol{\theta}_j) \equiv \tilde{\nabla} f(\boldsymbol{\theta}; \boldsymbol{\theta}_j)|_{\boldsymbol{\theta}=\boldsymbol{\theta}_i}$, where the operator $\tilde{\nabla}$ is defined as

$$\tilde{\nabla}_j \equiv (r^{-1}\partial_{\theta_1}, \xi_j^{-1}\partial_{\theta_2}) \,; \qquad \xi_j \equiv R + r\cos\theta_{1j} \,, \tag{1.5}$$

while $|\mathbf{x} - \mathbf{x}_j|_g$ for $\mathbf{x}$ near $\mathbf{x}_j$ is the geodesic distance from $\mathbf{x}$ to $\mathbf{x}_j$ with respect to the metric tensor g given by (1.2b). We remark that, unlike the case of the source-neutral Green's function on the surface of a sphere for which the regular part is constant [39, 25], R_N encodes the curvature of the torus; as a result, while a single spot remains stationary on the surface of a sphere, a single spot on the surface of a torus drifts to an equilibrium location. The numerical determination of the gradient of the regular part requires a detailed knowledge of the singularity behavior of G_N at $\boldsymbol{\theta}_j$. We demonstrate in §4 that the analytic-numerical algorithm introduced in §2 fulfills this need to a high degree of accuracy.

In §5, we analyze the stability of an equilibrium pattern characterized by a single spot located on the inner equator of the torus at $\theta_1 = \pi$. We consider locally radially symmetric amplitude perturbations, and find that a pair of complex eigenvalues crosses the imaginary axis at $\pm i\lambda_{H0}$ with $\lambda_{H0} \sim \mathcal{O}(1)$ as τ is increased past a certain threshold τ_{H0}. The instability results in growing oscillations in the amplitude of the spot.

In this analysis, we require detailed knowledge of the local behavior of the Helmholtz Green's function, given by the solution to

$$\Delta_g G_H - k G_H = -\delta(\boldsymbol{\theta}; \boldsymbol{\theta}_0) \,, \tag{1.6}$$

with appropriate periodicity conditions. We remark that, while conformal mapping and special function methods have been used to obtain an analytic formula for the source-neutral Green's function G_N (modulo

the integral condition of (1.3a)), such analytic techniques are not available for the Helmholtz Green's function satisfying (1.6). We demonstrate in §5 that the analytic-numerical technique introduced in §2 yields the desired quantities to a high degree of accuracy.

In §6 we consider the stability of a two-spot equilibrium pattern to a monotonic competition instability as the torus is slowly deformed. To determine the stability threshold, we require an accurate computation of $R_N(\mathbf{x}_0;\mathbf{x}_0)$ along with $G_N(\mathbf{x}_1;\mathbf{x}_0)$, where $\mathbf{x}_1 \neq \mathbf{x}_0$. We demonstrate that the analytic-numerical algorithm of §2 can yield sufficiently accurate values for these quantities to facilitate an accurate determination of the stability threshold.

We thus begin in §2 by introducing an analytic-numerical method for accurately computing a Green's function for lower order perturbations of the Laplacian on a curved surface. The method centers on a classical microlocal approach for analytically determining all (spatially varying) coefficients of singular terms proportional to $|\mathbf{x}-\mathbf{x}_0|_g^{2k}\log|\mathbf{x}-\mathbf{x}_0|_g$, $k=0,1,\ldots$, of the local behavior of the Green's function near the singular point $\mathbf{x}_0$. The method was developed by Hadamard to construct a parametrix for linear elliptic and hyperbolic PDEs, but we follow the presentation of Hörmander [15] in our work. To the best of our knowledge, this is the first work where microlocal techniques have been used to analyze pattern formation in nonlinear parabolic PDEs.

Because this singularity structure is constructed to be valid in a region around $\mathbf{x}_0$ (the precise extent of the region of validity, the injectivity radius, is given in §2), the resulting numerical problem is regular. That is, in order to obtain the Green's function, one need only solve a problem for $\tilde{r}(\theta)$ of the form $\Delta_g\tilde{r} - k\tilde{r} = R_1(\theta)$ with appropriate periodicity conditions, where the function $R_1(\theta)$, while computed numerically, is in principle as smooth as is desired. As a result, all the necessary information of the local behavior of the Green's function can be obtained by a combination of microlocal analysis and numerically via solution of a regular problem. We emphasize that the parametrix construction we use is classical and we refer the reader to [15] for a detailed exposition.

We remark that this method is useful for equations of the forms of both (1.3a) and (1.6); in practice, we observe that adding a small relaxation term ωG_N to the left-hand side of (1.3a), where $|\omega| \ll 1$ yields a sufficiently accurate approximation for G_N while enforcing the zero-mean condition of (1.3a). We further emphasize that this analytic-numerical technique can be applied to compute more general Green's functions satisfying equations of the form

$$(\Delta_g + X + V)G = -\delta(\mathbf{x};\mathbf{x}_0)\,, \tag{1.7}$$

for any metric tensor g, vector field X, and smooth function V (here, following differential geometry convention, "vector field" is understood as a first order differential operator [23]). As such, this method can be applied to analyze various reaction-diffusion systems with arbitrary advection along with spatially variable reaction and diffusion coefficients on curved open or closed surfaces. Such cases have recently been considered in 1- and 2-dimensional flat domains (see, e.g, [18, 21, 38, 3, 2, 34]).

The main goals of this paper are twofold. Primarily, we seek to introduce both the theoretical underpinnings of the abovementioned analytic-numerical method for computing Green's functions on curved surfaces and also a numerical recipe for its application in practice. While the microlocal analysis techniques presented here are classical dating back to Hadamard, we are unaware of existing literature which uses it to study this particular problem. Secondarily, we demonstrate its proficiency by using the recipe to obtain results for the dynamics and stability of localized spot patterns on the surface of a ring torus. Analysis of the latter relies critically on the ability to accurately compute certain quantities associated with Green's functions on the domain of interest. The majority of similar studies in the past have thus been limited to geometries on which Green's functions are analytically known, such as the disk [47, 20] and rectangle [20], surface of a sphere [32, 39], and the interior of a sphere [42]. We emphasize, though, that the hybrid asymptotic-numerical methods we use in §§3-6 have been developed in detail over all of these past works, beginning with that of Kolokolnikov et al. in 2009 [20], and are thus not new. To the best of our knowledge, however, the analytic-numerical method of §2, its coupling to the hybrid asymptotic-numerical method, and the results this framework yields regarding the impact of non-constant surface curvature on localized spot patterns, are all original.

2. The analytic-numerical approach to computing Green's functions on compact curved surfaces

Here we build the theoretical foundations for our analytic-numerical algorithm for obtaining the Green's function, with which we conclude in §2.4. All of the analytic and geometric techniques presented here are well-known in the geometric analysis community and can be found in [15]. We only present them here for the purpose of having a self-contained article.

We illustrate our strategy by considering the simplest example. For a fixed point $p_0 \in M$ we wish to numerically reconstruct the Green's function $G(p_0, p)$ for the operator $\Delta_g + 1$ by solving

$$(\Delta_g + 1)G(p_0, p) = \delta(p_0, p).$$

Numerically it is very difficult (and expensive) to approximate a δ-function, so we avoid the brute force approach. Instead, we first construct a "parametrix" u_{apprx} so that

$$(\Delta_g + 1)u_{apprx} = \delta(p_0, p) + R(p_0, p)\,,$$

where the remainder $R(p_0, p)$ is sufficiently regular for p near p_0. The method for construction of u_{apprx} involves only solving transport equations with smooth coefficients and can be done easily by integrating ODEs. Once u_{apprx} is constructed, all we need to do is to solve numerically for the correction u_{corr} by

$$(\Delta_g + 1)u_{corr} = -R(p_0, p)\,,$$

which has a very well behaved right-hand-side. The resulting $u_{apprx} + u_{corr}$ is the Green's function. Thus we are able to obtain the Green's function without having to numerically approximate singular objects.

2.1. **Geometric Preliminaries.**

The techniques we describe in this section are well-known in differential geometry (see [23] for a detailed reference) and we only present it for the convenience of the reader. In order to tap into the full power of the machinery of geometric PDE, we will need to use the language of intrinsic geometry, where the surface M is viewed as an object on its own rather than a hypersurface embedded in $\mathbb{R}^3$. We will also use standard differential geometry notation in the section.

The parametrization by (θ^1, θ^2) (following differential geometry convention, we use upper indices for this section and also forgo the bolding of vectors) can be viewed as a coordinate system for the open patch given by

$$\{\theta^1 \in (-\pi/2, 3\pi/2)\ , \theta^2 \in (0, 2\pi)\}\,.$$

These coordinates while intuitive are not very good at capturing the geometry of the surface. By "geometry" we mean a positive definite symmetric 2-tensor field g (which is called the "metric"). In our case our metric is given by the pullback of the Euclidean metric in $\mathbb{R}^3$ by the embedding $\iota : M \to \mathbb{R}^3$. This tensor gives a notion of an intrinsic distance between points on the surface. In the coordinates given by θ it takes on the form:

$$\tilde{g}_{j,k}(\theta)d\theta^k d\theta^j = r^2 d\theta^1 d\theta^1 + (R + r\cos\theta^1)^2 d\theta^2 d\theta^2. \tag{2.1}$$

The inverse of this matrix denoted by $\tilde{g}^{j,k}$ is given by $(\tilde{g}^{j,k}(\theta)) = \mathrm{diag}(r^{-2}, (R + r\cos\theta^1)^{-2})$.

Our first task is to make a change of coordinates so that the coordinate system accurately reflects the notion of distance. To do this, choose a point $p_0 \in M$ which corresponds to $\theta_0 \in \{\theta^1 \in (-\pi/2, 3\pi/2)\ , \theta^2 \in (0, 2\pi)\}$ and consider the map $x \mapsto \theta(x)$ for $x = (x^1, x^2) \in \mathbb{R}^2$ near the origin given by

$$\theta(x) = (\gamma^1(1), \gamma^2(1))\,, \tag{2.2}$$

where $(\gamma^1(t), \gamma^2(t), \xi_1(t), \xi_2(t))$ solves ODE systems

$$\dot{\gamma}^1(t) = r^{-2}\xi_1(t), \quad \dot{\gamma}^2(t) = (R + r\cos(\gamma^1(t)))^{-2}\xi_2(t), \ \dot{\xi}_1 = -\frac{(\xi_2(t))^2\,,\ r\sin(\gamma^1(t))}{(R + r\cos(\gamma^1(t)))^3}, \ \dot{\xi}_2 = 0\,,$$

with initial conditions $(\gamma^1(0), \gamma^2(0)) = (\theta_0^1, \theta_0^2)$ and $(\xi_1(0), \xi_2(0)) = (r^2 x^1, x^2(R + r\cos\theta_0^1)^2)$.

Clearly $\theta(0) = \theta_0$ and one can easily check by differentiating the dependence on the initial value (x^1, x^2) the Jacobian of this map is identity at $x = 0$. Therefore by the inverse function theorem, there exists

a smooth map $\theta \mapsto x(\theta)$ that is the inverse of the map $x \mapsto \theta(x)$. In fact, the map $x \mapsto \theta(x)$ is a diffeomorphism for $|x|_{\tilde{g}(\theta_0)} < r_{inj}$ where the "injectivity radius" is

$$r_{inj} = \min\{\pi\sqrt{r(R-r)}, \frac{R-r}{2}, \frac{r}{2}\}. \tag{2.3}$$

To see this, note that direct calculation shows that at a given θ the sectional curvature is given by $K(\theta) = \frac{\cos\theta^1}{r(R+r\cos\theta^1)}$ so that $|K(\theta)| \leq \frac{1}{r(R-r)}$. A direct application of [29, p. 178] gives the stated lower bound on the injectivity radius.

The nice thing about the coordinates given by x is that if $p \in M$ is a nearby point of p_0 and p corresponds to $\theta(x)$ then

$$d_g(p, p_0) = \left(x^k x^j \hat{g}_{j,k}\right)^{1/2}, \quad (\hat{g}_{j,k}) = \operatorname{diag}\left(r^2, (R + r\cos\theta_0^1)^2\right).$$

In addition, geodesics emanating from θ_0 are easy to describe in the x coordinate. They are simply curves given by $t \mapsto \theta(tx)$ for any $x \in \mathbb{R}^2$ small. That is, in the x coordinates, they are just straight radial lines emanating from the origin. For this reason the coordinate representation given by x defined above is often called "normal coordinates". In general these coordinates have the following property:

Lemma 2.1. *Let $\Psi_{p_0}(\cdot) = (x^1(\cdot), \ldots, x^n(\cdot))$ be a Riemann normal coordinate chosen at the point p_0 then we have, for p sufficiently close to p_0:*
i) $d_g(p_0, p)^2 = |x(p)|^2_{\hat{g}}$ where $|x|^2_{\hat{g}} := \hat{g}_{j,k}x^k x^j$,
ii) $g_{j,k}(p) = \hat{g}_{j,k} + O(|x(p)|^2_{\hat{g}})$
iii) $\hat{g}_{j,k}x^k(p) = g_{j,k}(x(p))x^k(p)$.

Proof. i) is a direct consequence of the definition of geodesic coordinates. ii) is the standard fact that in normal coordinates the Christoffel symbols vanish at the origin. iii) is a direct consequence of the Gauss lemma, which says that the the velocity of the geodesics is normal to the geodesic sphere. □

Let us discuss what happens to differential operators under this change of variable. Use $\tilde{\Psi}(\theta)$ to denote the coordinate map given by (1.1a) and set $\Psi(x) := \tilde{\Psi}(\theta(x))$. Suppose $\tilde{L}_{X,V}$ is the operator

$$\tilde{L}_{X,V} = -(R + r\cos\theta^1)^{-1}r^{-2}\partial_{\theta^1}(R + r\cos\theta^1)\partial_{\theta^1} - (R + r\cos\theta^1)^{-2}\partial^2_{\theta^2} + \tilde{b}^k(\theta)\partial_{\theta^k} + \tilde{V}(\theta)$$

then by the standard coordinate change formula we have for all $\tilde{u} \in C^\infty(\mathbb{R}^2)$

$$(\tilde{L}_{X,V}\tilde{u}) \circ \tilde{\Psi} \circ \Psi^{-1} = L_{X,V}u\,,$$

where $u = \tilde{u} \circ \tilde{\Psi} \circ \Psi^{-1}$ and

$$L_{X,V}u = \frac{-1}{\sqrt{|(g_{j,k})|}}\partial_{x^j}\left(\sqrt{|(g_{j,k})|}g^{j,k}\partial_{x^k}u\right) + b^k\partial_{x^k} + V\,,$$

with

$$g(x) := (g_{j,k}(x)) = \frac{{}^tD\theta}{Dx}\operatorname{diag}\left[r^2, \left(R + r\cos(\theta^1(x))\right)^2\right]\frac{D\theta}{Dx}\,, \tag{2.4}$$

$$b(x) = \left(\frac{D\theta}{Dx}\right)^{-1}\tilde{b}(\theta(x)), \quad V(x) = \tilde{V}(\theta(x))\,. \tag{2.5}$$

2.2. **Basis Distributions in $\mathbb{R}^n$.** We now construct a series of distributions on flat space that will serve as our basis for an singularity expansion. The basis we use is identical to the ones presented in [15].

2.2.1. *Basis Distributions via Fourier Tranform.* We construct distributions $\{F_j \mid j \in \mathbf{N}_0\}$ on $\mathbb{R}^2$ which satisfy globally the relation:

$$(\Delta + z)F_0 = \delta_0, \quad (\Delta + z)F_j = jF_{j-1} \quad j \geq 1\,, \tag{2.6}$$

and

$$-2\nabla F_j = xF_{j-1}, \quad j \geq 1\,, \quad \nabla F_0 = \frac{x}{2}\int \log(z + |\xi|^2)e^{ix\cdot\xi}d\xi\,, \tag{2.7}$$

for $z \in \mathbf{C}\backslash\mathbb{R}_-$. In fact, only F_0 will be a distribution while all other F_j will be C^1 functions. These are quite easy to construct via the Fourier transform:

$$F_j(x) = \frac{j!}{(2\pi)^n}\int \frac{e^{ix\cdot\xi}}{(z + |\xi|^2)^{j+1}}d\xi.$$

To simplify notation we will mostly suppress the dependence on z. In discussions where the dependence on z becomes relevant we will write $F_j(x; z)$ or F_j^z.

It is easily seen by integrability argument and basic Lebesgue theory that when $n = 2$, F_0 is a tempered distribution, $F_1 \in H^1(\mathbb{R}^2) \cap C^1(\mathbb{R}^2)$, and

$$F_j \in H^{2j-1}(\mathbb{R}^2) \cap C^{2j-1}(\mathbb{R}^2)\,, \tag{2.8}$$

for all $j \geq 2$. Furthermore, by repeated integrations by parts we can see that

$$F_j \in C^\infty(\mathbb{R}^2\backslash\{0\})\,, \tag{2.9}$$

for all j. Indeed, we can write

$$e^{ix\cdot\xi} = |x|^{-2}\Delta_\xi e^{ix\cdot\xi} = |x|^{-2k}\Delta_\xi^k e^{ix\cdot\xi}\,,$$

in the integrand and integrate by parts in ξ:

$$F_j(x) = |x|^{-2k}\frac{j!}{(2\pi)^n}\int_\xi e^{ix\cdot\xi}\Delta_\xi^k\left(\frac{1}{(z + |\xi|^2)^{j+1}}\right). \tag{2.10}$$

Note that $\Delta_\xi^k(z + |\xi|^2)^{-j-1}$ decays like $(z + |\xi|^2)^{-j-1-k}$ and therefore the integral in ξ decays sufficiently quickly out at infinity and we can differentiate under the integral by standard Lebesgue theory as long as $x \neq 0$.

For the distribution F_0 we can work out the form of the singularity at the origin:

Lemma 2.2. *The distribution F_0 satisfies that for any $\chi \in C_c^\infty(\mathbb{R}^2)$ which is identically 1 near the origin,*

$$\chi(F_0 + \frac{1}{2\pi}\log|x|) \in C_c^{1,\gamma}(\mathbb{R}^2). \tag{2.11}$$

Proof. Observe that $\Delta \log|x| = -2\pi\delta_0$ so if we apply $\Delta + z$ to $\chi(F_0 + \frac{1}{2\pi}\log|x|)$ we get

$$(\Delta + z)\chi(F_0 + \frac{1}{2\pi}\log|x|) = [\Delta, \chi](F_0 + \frac{1}{2\pi}\log|x|) + \frac{z}{2\pi}\chi\log|x|.$$

The first term is actually in $C_c^\infty(\mathbb{R}^2)$ since the coefficients of the commutator $[\Delta, \chi]$ are supported away from the origin. The second term is in $L^p(\mathbb{R}^2)$ for all $p \in (1, \infty)$. Standard elliptic theory in conjunction with Sobolev embedding then shows that $\chi(F_0 + \frac{1}{2\pi}\log|x|) \in C^{1,\gamma}(\mathbb{R}^2)$. □

Using (2.10) we can also show

Lemma 2.3. *The distributions F_j satisfy $|x|F_j(x) \in L^1_{loc}$.*

It turns out that $F_j(x)$ are radial distributions:

Lemma 2.4. *The distributions $F_j(x)$ are invariant under action by $O(n, \mathbb{R})$. That is, $F_j(x) = F_j(|x|)$.*

Proof. Let A be any orthogonal matrix. Then for all $x \neq 0$

$$F_j(Ax) = \frac{j!}{(2\pi)^n} \int \frac{e^{iAx\cdot\xi}}{(z+|\xi|^2)^{j+1}} d\xi.$$

Make a change of variable $\xi \mapsto A\xi$ and use the fact that $|\xi| = |A\xi|$, $|\det A| = 1$ since A is orthogonal. This means that $F_j(x^1, \ldots, x^n) = F_j(|x|, 0, \ldots, 0)$ for all $x \in \mathbb{R}^2 \backslash \{0\}$. □

Remark 1. *Due to this proposition we will sometimes write $F_j = F_j(x) = F_j(|x|)$.*

We like to modify F slightly so that it is compatible with the metric $g_{j,k}(x)$ at the origin. Let $T : \mathbb{R}^2 \to \mathbb{R}^2$ be a linear bijection such that $g^{j,k}(0) := \hat{g}^{j,k} = (T^t T)^{-1}$. Then $|Tx| = |x|_{\hat{g}}$ and setting

$$T^* F(x) := F(Tx) = F(|x|_{\hat{g}}), \tag{2.12}$$

(2.6), (2.7) becomes

$$(-\partial_{x^k} \hat{g}^{j,k} \partial_{x^j} + z) T^* F_0 = |\hat{g}|^{-1/2} \delta_0, \quad (-\partial_{x^k} \hat{g}^{l,k} \partial_{x^l} + z) T^* F_j = j T^* F_{j-1} \quad j \geq 1\,, \tag{2.13}$$

and

$$-2\hat{g}^{l,k} \partial_{x^l} T^* F_j = x^k T^* F_{j-1} \quad j \geq 1, \quad \hat{g}^{l,k} \partial_{x^l} T^* F_0(x) = \frac{x^k}{2} \int \log(z+|\xi|^2) e^{iTx\cdot\xi}. \tag{2.14}$$

The relations (2.13) and (2.14) can be verified in the sense of distributions by direct computation.

2.3. **Hadamard Parametrix.** We proceed as in [15] to derive a singularity expansion in terms of $\{F_j\}$ for the Green's function of $G(p_0, p)$ of $\Delta_g + X + V$ for p near p_0. Here X is a smooth vector field and V is a smooth function. Let us fix p_0 and choose normal coordinates $(\Psi_{p_0}(p), U)$ where

$$\Psi_{p_0}(p) = (x^1(p), \ldots, x^n(p)), \Psi_{p_0}(p_0) = 0.$$

Let $g_{j,k}(x) dx^j dx^k$ be the coordinate expression for this metric with $g_{j,k}(0) = \hat{g}_{j,k}$. In these coordinates the operator Δ_g has the form, for all $u \in C_c^\infty(\Psi(U))$,

$$\Delta_g (u \circ \Psi)(p) = -\Big(\partial_j g^{j,k}(x) \partial_k u - (\partial_j \log |g(x)|) g(x)^{j,k} \partial_k u \Big) \mid_{x=\Psi(p)},$$

where $g^{j,k}$ is the inverse of $g_{j,k}$ and $|g(x)|$ is the determinant of the matrix $g_{j,k}(x)$. We say that in the coordinate Ψ, Δ_g is given by

$$\Delta_g = -\partial_j g^{j,k}(x) \partial_k - (\partial_j \log \sqrt{|g(x)|}) g^{j,k} \partial_k.$$

Furthermore, let $b^k \partial_k$ be the expression of X in this coordinate. Therefore, if $\alpha_0(x) F_0(|x|_{\hat{g}}) + \cdots + \alpha_N(x) F_N(|x|_{\hat{g}})$ is an asymptotic expansion for the Green's function of the differential operator

$$L_{X,V} := -\partial_j g^{j,k}(x) \partial_k - g^{j,k}(x) (\partial_j \log \sqrt{|g(x)|}) \partial_k + b^k \partial_k + V\,, \tag{2.15}$$

for $x \in \Psi(U)$, then using Lemma 2.1 we have that $G(p_0, p)$ has asymptotic

$$\alpha_0 \circ \Psi(p) F_0(d_g(p_0, p)) + \cdots + \alpha_N \circ \Psi(p) F_N(d_g(p_0, p)).$$

2.3.1. *Preliminary Calculations.* Let us carry out this computation by first computing $(-\partial_j g^{j,k}(x) \partial_k + z) F_m(|x|_{\hat{g}})$. For $x \neq 0$, the distribution $F_m(|x|_{\hat{g}})$ is actually smooth by (2.9), so we can compute directly

$$g^{j,k}(x) \partial_k F_m(|x|_{\hat{g}}) = g^{j,k}(x) \frac{\hat{g}_{l,k} x^l}{|x|_{\hat{g}}} F_m'(|x|_{\hat{g}}).$$

Now we will use the fact that $g_{j,k}(x)$ is in the metric expression in normal coordinates and evoke Lemma 2.1. Indeed Lemma 2.1 allows us to write $\hat{g}_{l,k} x^l = g_{l,k}(x) x^l$ and substitute this into the above expression:

$$g^{j,k}(x) \partial_k F_m(|x|_{\hat{g}}) = g^{j,k}(x) g_{l,k}(x) \frac{x^l}{|x|_{\hat{g}}} F_m'(|x|_{\hat{g}}) = \frac{x^j}{|x|_{\hat{g}}} F_m'(|x|_{\hat{g}}) = \hat{g}^{j,k} \partial_k F_m(|x|_{\hat{g}})\,,$$

for all $x \neq 0$. We claim that this expression holds on $\mathbb{R}^n$ in the sense of distributions:

Lemma 2.5. *For all $u \in C_c^\infty(\mathbb{R}^n)$,*

$$\int u(x) g^{j,k}(x) \partial_k F_m(|x|_{\hat{g}}) dx = \int u \hat{g}^{j,k} \partial_k F_m(|x|_{\hat{g}}).$$

That is, $g^{j,k}(x)\partial_k F_m(|x|_{\hat{g}}) = \hat{g}^{j,k}\partial_k F_m(|x|_{\hat{g}})$ in the sense of distributions.

Proof. To simplify notation we prove this for $\hat{g}^{j,k} = \delta^{j,k}$. Let $\chi \in C_c^\infty(\mathbb{R}^n)$ be identically 1 near the origin and write $\chi_\epsilon(x) = \chi(x/\epsilon)$. We then have that

$$\begin{aligned}\int u(x) g^{j,k}(x) \partial_k F_m(|x|) dx &= \int \chi_\epsilon(x) u(x) g^{j,k}(x) \partial_k F_m(|x|) dx \\ &\quad + \int (1-\chi_\epsilon(x)) u(x) g^{j,k}(x) \partial_k F_m(|x|) dx.\end{aligned}$$

The integrand in the second term is away from $x = 0$ so we can apply the identity directly to obtain

$$\begin{aligned}\int u(x) g^{j,k}(x) \partial_k F_m(|x|) dx &= \int \chi_\epsilon(x) u(x) g^{j,k}(x) \partial_k F_m(|x|) dx \\ &\quad + \int (1-\chi_\epsilon(x)) u \delta^{j,k} \partial_k F_m(|x|) dx.\end{aligned}$$

For the first integral we again use the fact that we are using geodesic coordinate so that for $x \in \mathrm{supp}(\chi_\epsilon)$, $g^{j,k}(x) = \delta^{j,k} + f^{j,k}(x)$ for some smooth $f^{j,k}(x)$ with $f^{j,k}(0) = \nabla f^{j,k}(0) = 0$. Substituting this into the above expression we have

$$\begin{aligned}\int u(x) g^{j,k}(x) \partial_k F_m(|x|) dx &= \int \chi_\epsilon(x) u(x) f^{j,k}(x) \partial_k F_m(|x|) dx \\ &\quad + \int u \delta^{j,k} \partial_k F_m(|x|) dx.\end{aligned}$$

Integrate the first term by parts (in fact this is how distributions are defined), we get

$$\begin{aligned}\int u(x) g^{j,k}(x) \partial_k F_m(|x|) dx &= \int (\chi_\epsilon(x) u(x) \partial_k f^{j,k}(x) + \chi_\epsilon(x) \partial_k u(x) f^{j,k}(x) \\ &\quad + \epsilon^{-1} \chi_k(\frac{x}{\epsilon}) u(x) f^{j,k}(x)) F_m(|x|) dx \\ &\quad + \int u \delta^{j,k} \partial_k F_m(|x|) dx\,,\end{aligned}$$

where $\chi_k := \partial_k \chi$. One can then easily show that when $\epsilon \to 0$

$$\int (\chi_\epsilon(x) u(x) \partial_k f^{j,k}(x) + \chi_\epsilon(x) \partial_k u(x) f^{j,k}(x) + \epsilon^{-1} \chi_k(\frac{x}{\epsilon}) u(x) f^{j,k}(x)) F_m(|x|) dx \to 0\,,$$

by using the fact that $|f^{j,k}(x)| \le C|x|^2$, Lemma 2.3, and standard Lebesgue theory. □

Owing to Lemma 2.5 and (2.13) we have that, for x near the origin,

$$(-\partial_j g^{j,k}(x)\partial_k + z) F_0(|x|_{\hat{g}}) = |\hat{g}|^{-1/2}\delta_0,\ (-\partial_j g^{j,k}(x)\partial_k + z) F_m(|x|_{\hat{g}}) = m F_{m-1}(|x|_{\hat{g}})\,, \tag{2.16}$$

for $m \ge 1$. Furthermore, using Lemma 2.5 in conjunction with (2.14) we obtain

$$g^{j,k}(x)\partial_k F_0(|x|_{\hat{g}}) = \hat{g}^{j,k}\partial_k F_0(|x|_{\hat{g}}),\ g^{j,k}(x)\partial_k F_m(|x|_{\hat{g}}) = -\frac{x^j}{2} F_{m-1}(|x|_{\hat{g}}). \tag{2.17}$$

2.3.2. *Solving for Leading Term.* Let α_0 be a smooth function on $\mathbb{R}^n$ and hit $\alpha_0(x) F_0(|x|_{\hat{g}}) = \alpha_0 T^* F_0$ by the operator L defined in (2.15). Using (2.16) and (2.17)

$$\begin{aligned}L_{X,V}(\alpha_0 T^* F_0) &= \alpha_0 |\hat{g}|^{-1/2}\delta_0 - T^* F_0 \partial_k (g^{j,k}(x)\partial_j \alpha_0) \\ &\quad -2\hat{g}^{j,k}\partial_j T^* F_0 \partial_k \alpha_0 - T^* F_0 g^{j,k}(x) \partial_k \log\sqrt{|g(x)|}\partial_j \alpha_0 \\ &\quad -\alpha_0 \hat{g}^{j,k}\partial_k \log\sqrt{|g(x)|}\partial_j T^* F_0 + (V - z) T^* F_0 \\ &\quad + T^* F_0 b^k \partial_k \alpha_0 + \alpha_0 b^k \partial_k T^* F_0.\end{aligned}$$

Note that if we simply choose α_0 to solve

$$\alpha_0 x^j \hat{g}_{j,k} b^k - \alpha_0 x^k \partial_k \log \sqrt{|g(x)|} = 2x^k \partial_k \alpha_0, \tag{2.18}$$

which can be accomplished by setting

$$\alpha_0(x) := |g(x)|^{-1/4} |\hat{g}|^{1/4} \exp\left(\int_0^1 \frac{x^j \hat{g}_{j,k} b^k(tx)}{2} dt \right), \tag{2.19}$$

the terms involving $\partial_j F_0$ drop out and we get

$$L_{X,V}(\alpha_0 T^* F_0) = |\hat{g}|^{-1/2} \delta_0 + e_0 T^* F_0 \tag{2.20}$$

where

$$\begin{aligned} e_0(x) \;:=\; & -\partial_k (g^{j,k}(x) \partial_j \alpha_0(x)) - g^{j,k}(x) (\partial_k \log \sqrt{|g(x)|}) (\partial_j \alpha_0(x)) \\ & + (V(x) - z)\alpha_0 + b^k(x) \partial_k \alpha_0(x). \end{aligned} \tag{2.21}$$

Observe that when $X = 0$ (i.e. $b = 0$), (2.19) shows that

$$\alpha_0(x) = 1 + O(|x|^2), \tag{2.22}$$

due to Lemma 2.1 ii). Note that if we are given an explicit expression for $g_{j,k}(x)$, we can write down explicitly what α_0 and e_0 are. We would like to eliminate all the terms after δ_0 in (2.20). This leads us to the next subsection.

2.3.3. *Solving for Subsequent Terms.* Suppose we have computed explicitly $\alpha_0, \ldots, \alpha_{m-1}$ for some $m \geq 1$ such that

$$L_{X,V}(\alpha_0 F_0 + \cdots + \alpha_{m-1} F_{m-1}) = |\hat{g}|^{-1/2} \delta_0 + e_{m-1}(x) F_{m-1}. \tag{2.23}$$

with

$$\begin{aligned} e_{m-1}(x) \;=\; & -\partial_k (g^{j,k}(x) \partial_j \alpha_{m-1}(x)) - g^{j,k}(x) (\partial_k \log \sqrt{|g(x)|}) (\partial_j \alpha_{m-1}(x)) \\ & + (V(x) - z) + b^k(x) \partial_k \alpha_{m-1}(x). \end{aligned} \tag{2.24}$$

We now give an explicit construction of α_m in terms of $g_{j,k}$ and e_{m-1} such that (2.23) and (2.24) hold with m replacing $m-1$.

Computing $L_\lambda(\alpha_m F_m)$ for $m \geq 1$ using (2.16) and (2.17) gives

$$\begin{aligned} L_{X,V}(\alpha_m T^* F_m) \;=\; & m\alpha_m T^* F_{m-1} - T^* F_m \partial_k g^{j,k}(x) \partial_j \alpha_m + x^k T^* F_{m-1} \partial_k \alpha_m \\ & - T^* F_m g^{j,k}(x) \partial_k \log \sqrt{|g(x)|} \partial_j \alpha_m + \frac{\alpha_m}{2} x^k \partial_k \log \sqrt{|g(x)|} T^* F_{m-1} \\ & + (V - z) T^* F_m + T^* F_m b^k \partial_k \alpha_m - \alpha_m \frac{T^* F_{m-1}}{2} x^j \hat{g}_{j,k} b^k. \end{aligned} \tag{2.25}$$

If we can find smooth function α_m solving

$$2m\alpha_m + 2x^k \partial_k \alpha_m + \alpha_m x^k \partial_k \log \sqrt{|g(x)|} - \alpha_m x^j \hat{g}_{j,k} b^k + 2e_{m-1} = 0, \tag{2.26}$$

then (2.23) and (2.24) would hold with m in place of $m-1$.

Finding an explicit solution for the transport equation (2.26) is standard by taking as in [15]

$$\alpha_m(x) := -\alpha_0(x) \int_0^1 t^{m-1} e_{m-1}(tx)/\alpha_0(tx) dt. \tag{2.27}$$

One can then easily verify that $L_{X,V} \sum_{j=0}^m \alpha_j F_j = |\hat{g}|^{-1/2} \delta_0 + e_m F_m$ with

$$\begin{aligned} e_m(x) \;=\; & -\partial_k (g^{j,k}(x) \partial_j \alpha_m(x)) - g^{j,k}(x) (\partial_k \log \sqrt{|g(x)|}) (\partial_j \alpha_m(x)) \\ & + (V(x) - z)\alpha_m + b^k(x) \partial_k \alpha_m(x). \end{aligned} \tag{2.28}$$

We emphasize again that since $\alpha_0, \ldots, \alpha_{m-1}$ and $e_0, \ldots, e_{m-1}$ are constructed explicitly, both α_m and e_m are again explicit, and so this process can continue inductively to find exact formulae for as many α_m as we wish.

2.3.4. *Solving for the Smooth Remainder.* We now use the coordinate transform to define a parametrix that approximates the Green's function for the operator $\Delta_g + X + V$ on M. Suppose we have constructed

$$Q_N(x) := \sum_{j=0}^{N} \alpha_j(x) F_j(Tx) = \sum_{j=0}^{N} \alpha_j(x) F_j(|x|_{\hat{g}}) \,, \tag{2.29}$$

such that $L_{X,V} Q_N(x) = |\hat{g}|^{-1/2}\delta_0 + e_N(x) F_N(|x|_{\hat{g}})$ on $\mathbb{R}^n$ with e_N given by (2.24). Let $\chi \in C_c^\infty(\mathbb{R}^n)$ be a smooth cutoff radially concentric around the origin and Ψ be the normal coordinate around $p_0 \in M$. If $(\tilde{U}, \tilde{\Psi})$ is any other coordinate chart around p_0 containing U, we have that for any distribution u supported in $\Psi(U)$,

$$\tilde{L}_{X,V} \tilde{u} = (L_{X,V} u) \circ \Psi \circ \tilde{\Psi}^{-1} \,,$$

where $\tilde{u} := u \circ \Psi \circ \tilde{\Psi}^{-1}$ and $\tilde{L}_{X,V}$ is the coordinate expression of the operator $\Delta_g + X + V$ in the $\tilde{\Psi}$ coordinate. In particular, if we choose $u := \chi Q_N$ we then have that

$$\tilde{L}_{X,V} \tilde{u} = |\hat{g}|^{-1/2}\delta_0 \circ \Psi \circ \tilde{\Psi}^{-1} + (\chi e_N T^* F_N + [L_{X,V}, \chi] Q_N) \circ \Psi \circ \tilde{\Psi}^{-1}.$$

In particular if we find $\tilde{r}$ solving

$$\tilde{L}_{X,V} \tilde{r} = -(\chi e_N T^* F_N + [L_{X,V}, \chi] Q_N) \circ \Psi \circ \tilde{\Psi}^{-1} \,, \tag{2.30}$$

then $\tilde{L}_{X,V}(\tilde{u} + \tilde{r}) = |\hat{g}|^{-1/2}\delta_0 \circ \Psi \circ \tilde{\Psi}^{-1}$. This is understood in the sense that for any test function $\tilde{\varphi} \in C_c^\infty(\tilde{\Psi}(\tilde{U}))$

$$\int_{\tilde{\Psi}(\tilde{U})} \tilde{\varphi} \tilde{L}_{X,V}(\tilde{u} + \tilde{r}) \sqrt{|\tilde{g}|} d\tilde{x}^1 \dots d\tilde{x}^n = \tilde{\varphi} \circ \tilde{\Psi} \circ \Psi^{-1}(0).$$

2.3.5. *Regularity of the Remainder.* Suppose we have constructed $\alpha_0(x), \dots, \alpha_N(x)$ for $x \in \mathbb{R}^n$ near the origin such that

$$L_{X,V}(\sum_{j=0}^{N} \alpha_j F_j) = \delta_0 + e_N F_N \,,$$

with e_N given by (2.24).

We would like to see how closely

$$\sum_{j=0}^{N} \alpha_j \circ \Psi(p) F_j \circ \Psi(p) \,,$$

approximates the actual Green's function $G_{X,V}(p_0, p)$ near p_0 in terms of regularity. Here $\Psi(\cdot) : U \to \Psi(U) \subset \mathbb{R}^n$ is a normal coordinate centered at p_0, which takes p_0 to the origin (actually $\Psi(\cdot) = \Psi_{p_0}(\cdot)$) since the coordinate map depends on the centre point p_0 chosen. However, writing it in this way would make the notation much too cumbersome).

To this end we fix p_0 and choose a smooth cutoff χ which is identically 1 near p_0 and supported inside the coordinate neighbourhood U. Define $G(x) := \chi \circ \Psi^{-1}(x) G_{X,V}(p_0, \Psi^{-1}(x))$. We then have that

$$L_{X,V} G(x) = \delta_0 + [L_{X,V}, \chi \circ \Psi^{-1}(x)] G_{X,V}(p_0, \Psi^{-1}(x)).$$

The term involving the commutator is again smooth since the only singularity of $G_{X,V}(p_0, \Psi^{-1}(x))$ is when $x = 0$ and the coefficients of $[L_{X,V}, \chi \circ \Psi^{-1}(x)]$ are supported away from there. Therefore,

$$L_{X,V}(G(x) - \chi \circ \Psi^{-1}(x) \sum_{j=0}^{N} \alpha_j(x) F_j(x)) = \chi \circ \Psi^{-1}(x) e_N(x) F_N(x) + C_c^\infty(\mathbb{R}^n).$$

In particular when $N = 0$ this means $L_{X,V}(G(x) - \chi \circ \Psi^{-1}(x) \alpha_0(x) F_0(x)) \in L^p(\mathbb{R}^2)$ by Lemma 2.11 for all $p \in (0, 1)$. Elliptic regularity then yields that

$$G(x) - \chi \circ \Psi^{-1}(x) \alpha_0(x) F_0(x) \in W_c^{2,p}(\mathbb{R}^2) \,,$$

for all $p \in (1, \infty)$ which embeds into $C_c^{1,\gamma}(\mathbb{R}^2)$ for all $\gamma < 1$. Precomposing with $\Psi(\cdot)$ we get that

$$\chi(p)(G_{X,V}(p_0, p) - \alpha_0 \circ \Psi(p) F_0(d_g(p_0, p)) \in C_c^{1,\gamma}(M).$$

Here we have used the fact that $F_j(\Psi(p)) = F_j(|\Psi(p)|) = F_j(d_g(p_0, p))$ by Lemma 2.1.

Now by (2.22) we have that if $X = 0$ then $\alpha_0 \circ \Psi(p) = 1 + O(d_g(p, p_0)^2)$ when p is near p_0. Combining this fact with Lemma 2.11, we have that

$$\chi(p)(G_{0,V}(p_0, p) + \frac{1}{2\pi} \log d_g(p, p_0)) \in C_c^{1,\gamma}(M).$$

We have thus shown the classical result (see e.g. [15])

Proposition 2.1. *When the vector field X vanishes everywhere, we have that*

$$\chi(p)(G_{0,V}(p_0, p) + \frac{1}{2\pi} \log d_g(p, p_0)) \in C_c^{1,\gamma}(M).$$

2.4. **Algorithm for Computing Green's function for $\tilde{L}_{X,V}$ on the torus.** We summarize the above procedure in the following alogrithm:

I Assume that 0 is not an eigenvalue of the operator

$$\begin{aligned} \tilde{L}_{X,V} &= -(R + r\cos\theta^1)^{-1} r^{-2} \partial_{\theta^1} (R + r\cos\theta^1) \partial_{\theta^1} - (R + r\cos\theta^1)^{-2} \partial_{\theta^2}^2 \\ &\quad + \tilde{b}^k(\theta) \partial_{\theta^k} + \tilde{V}(\theta). \end{aligned}$$

Given a point $p_0 \in \mathbf{T}_{R,r}$ corresponding to the angles $(\theta_0^1, \theta_0^2) \in (-\pi/2, 3\pi/2) \times (0, 2\pi)$, set the constant (though depending on θ_0) matrix

$$\hat{g}_{j,k} = \mathrm{diag}[r^2, (R + r\cos\theta_0^1)^2].$$

Every quantity appearing below except for $F_j(x)$ depends on θ_0.

II Compute the change of variable $\theta(x)$ by (2.2). Compute its Jacobian and the inverse of the Jacobian.

III Compute the matrix $g_{j,k}(x)$, the vector $b(x)$, the potential $V(x)$ using (2.4) and (2.5). Set

$$L_{X,V} := -\partial_j g^{j,k}(x) \partial_k - g^{j,k}(x)(\partial_j \log \sqrt{|g(x)|}) \partial_k + b^k \partial_k + V\,.$$

IV Set $\alpha_0(x)$ as in (2.19) and $e_0(x)$ as in (2.21).

V Having constructed $\alpha_0, \ldots, \alpha_{m-1}$ and $e_0, \ldots, e_{m-1}$ construct α_m and e_m using (2.27) and (2.28).

VI Set $Q_N(x) := \sum_{j=0}^N \alpha_j(x) F_j(Tx)$ where T is the matrix $\mathrm{diag}[r, (R + r\cos\theta_0^1)]$. Note that dependence of θ_0 is hidden in T so $F_j(Tx)$ are functions of θ_0 as well.

VII Let $\chi(x) \in C_c^\infty(\mathbb{R}^2)$ be concentric around the origin such that $\chi(x) = 1$ for $|x|_{\hat{g}} \le \frac{r_{inj}}{4}$ and $\mathrm{supp}\chi \subset \{|x|_{\hat{g}} < \frac{r_{inj}}{2}\}$ where r_{inj} is given by (2.3). Compute

$$R_1 := [L_{X,V}, \chi] Q_N(x)\,.$$

VIII Compute $x = x(\theta)$, the inverse map of $\theta(x)$ on the set where $|x|_{\hat{g}} < r_{inj}/2$.

IX Compute $\tilde{r}(\theta^1, \theta^2)$ by solving numerically the PDE,

$$\tilde{L}_{X,V} \tilde{r} = -\chi(x(\theta)) e_N(x(\theta)) F_N(Tx(\theta)) - R_1(x(\theta))\,,$$

with periodic boundary conditions on the boundary of $(-\pi/2, 3\pi/2) \times (0, 2\pi)$.

X The function $\chi(x(\theta)) \sum_{m=0}^N \alpha_m(x(\theta)) F_m(Tx(\theta)) + \tilde{r}(\theta)$ is the Green's function $\tilde{G}_{X,V}(\theta_0, \theta)$ for $\tilde{L}_{X,V}$.

Below, as functions of $\theta = (\theta^1, \theta^2)$, we plot quantities obtained in key steps of the algorithm for the case $N = 1$ and $\theta_0 = (\pi, \pi)$ (i.e., on the inner equator of the torus). In Fig. 1(a), we show the smooth nonhomogeneous right-hand side of Step IX, onto which we invert the operator $\tilde{L}_{X,V}$ to obtain $\tilde{r}(\theta)$. It is equal to zero outside of the support of χ. With $N = 1$, the most singular term in this function is proportional to $|\mathbf{x} - \mathbf{x}_0|_g^2 \log |\mathbf{x} - \mathbf{x}_0|_g$, where $|\mathbf{x} - \mathbf{x}_0|_g$ is the geodesic distance from between the points $\mathbf{x}$ and $\mathbf{x}_0$ on torus, and $\mathbf{x}_0$ is the location of the delta source.

In Fig. 1(b), we plot the function $\chi(x(\theta)) \sum_{m=0}^{1} \alpha_m(x(\theta)) F_m(Tx(\theta))$, which contains the two most singular terms the Green's function constructed in Steps IV - VI. In particular, the logarithmic behavior is contained in F_0, which is simply the zeroth order modified bessel function of the second kind. As such, the logarithmic behavior of $\tilde{G}_{X,V}$ is constructed exactly. In Fig. 1(c), we plot the smooth remainder $\tilde{r}(\theta)$, obtained in Step IX by inversion of the operator $\tilde{L}_{X,V}$ with a basic finite difference method. Finally, in Fig. 1(d), we show $\tilde{G}_{X,V}(\theta_0, \theta)$, the sum of the functions shown in Fig. 1(b) and 1(c).

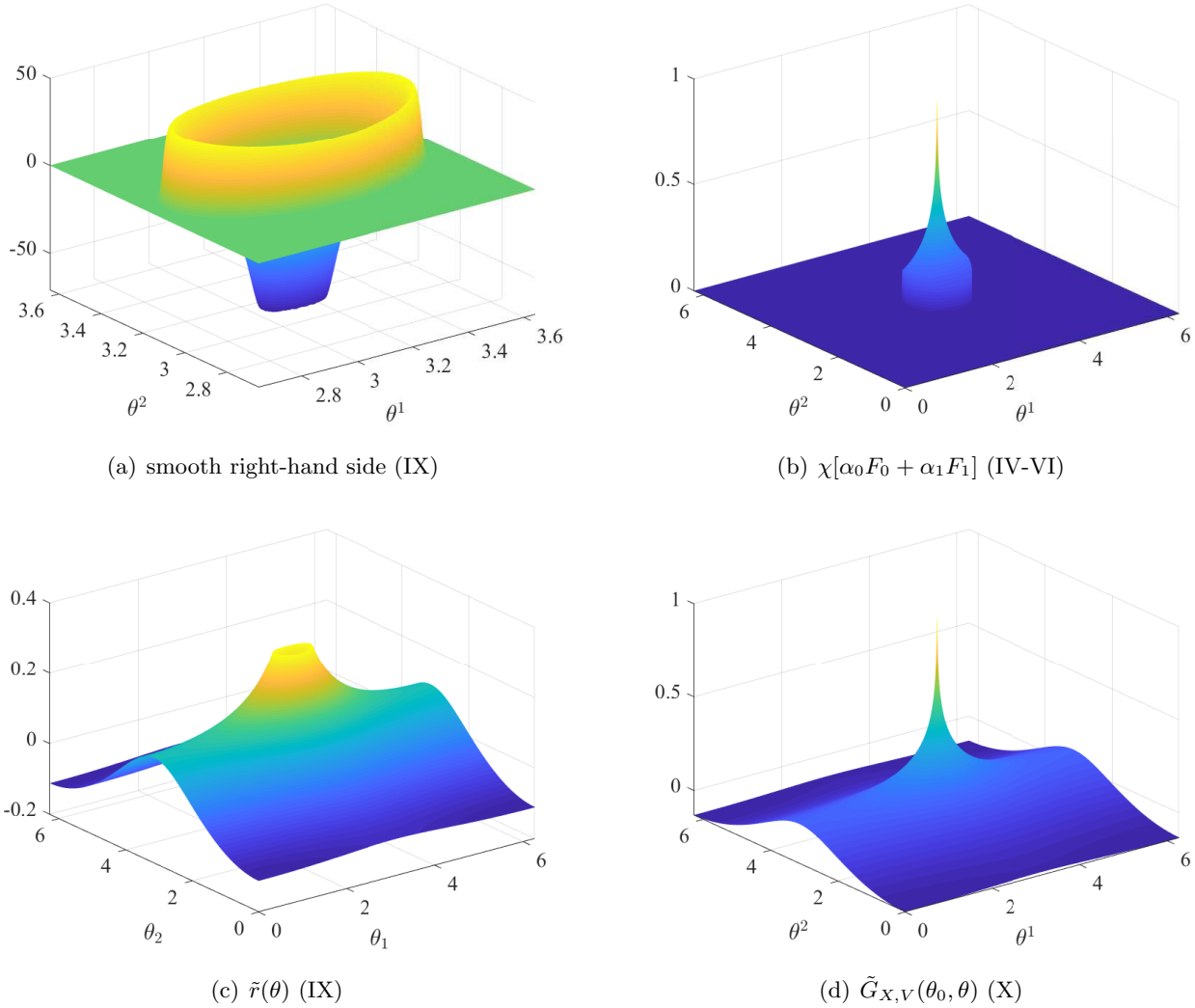

(a) smooth right-hand side (IX)

(b) $\chi[\alpha_0 F_0 + \alpha_1 F_1]$ (IV-VI)

(c) $\tilde{r}(\theta)$ (IX)

(d) $\tilde{G}_{X,V}(\theta_0, \theta)$ (X)

FIGURE 1. Plots of key quantities obtained in the algorithm of §2.4 for $N = 1$ and source location $\theta_0 = (\pi, \pi)$. (a) The nonhomogeneous right-hand side of Step IV. When $N = 1$, the most singular term is $|\mathbf{x} - \mathbf{x}_0|_g^2 \log |\mathbf{x} - \mathbf{x}_0|_g$. (b) Plot of $\chi(x(\theta)) \sum_{m=0}^{1} \alpha_m(x(\theta)) F_m(Tx(\theta))$, constructed in Steps IV - VI, and which contain the two most singular terms in $\tilde{G}_{XV}$. (c) The smooth remainder $\tilde{r}$ obtained in Step IX. (d) The full Green's function $\tilde{G}_{XV}$, obtained in Step X by adding the functions in (b) and (c).

3. N-SPOT QUASI-EQUILIBRIUM CONSTRUCTION

Because the following procedure and analysis for constructing a localized N-spot quasi-equilibrium has been performed in detail in past works for flat domains, 3-D domains, and the surface of a sphere (see, e.g., [39, 32, 8, 20, 42]), we omit many of the details. The primary goal of this section is instead to demonstrate that the asymptotic formulation, coupled with the analytic-numerical method for computing the source-neutral Green's function of (1.3a), yields an accurate approximation for quasi-equilibrium solutions of (1.2) that agree with the true numerical solution. For this reason, we will not appeal to the analytic formula for G_N on the surface of a ring torus computed in [12] using conformal mapping and special function methods. Furthermore, for the stability analysis of §5, for which the Helmholtz Green's function G_H of (1.6) is required, the method of [12] is no longer available. We emphasize that, because our method is a mix of numerical and analytic techniques, it is applicable to a far greater class of operators and surfaces than are purely analytic methods.

Following, e.g., [32], we construct a quasi-equilibrium solution by solving a certain inner problem for u and v in each of the $\mathcal{O}(\varepsilon)$ regions near $\mathbf{x}_j \equiv ((R + r\cos\theta_{1j})\cos\theta_{2j}, (R + r\cos\theta_{1j})\sin\theta_{2j}, r\sin\theta_{1j})$, $j = 1, \ldots, N$, and matching the solution in each inner region to the global outer solution for u. To begin, we define the two inner variables

$$y_{1j} = \frac{r(\theta_1 - \theta_{1j})}{\varepsilon}\,, \quad y_{2j} = \frac{\xi_j(\theta_2 - \theta_{2j})}{\varepsilon}\,; \qquad \mathbf{y}_j \equiv (y_{1j}, y_{2j}) \tag{3.1a}$$

along with

$$u(\boldsymbol{\theta} + \varepsilon\mathbf{y}_j) = U_j(\mathbf{y}_j)\,, \qquad v(\boldsymbol{\theta} + \varepsilon\mathbf{y}_j) = V_j(\mathbf{y}_j)\,. \tag{3.1b}$$

From the change of coordinates (3.1a), we have that for $\mathbf{x}$ near $\mathbf{x}_0$, the geodesic distance $|\mathbf{x} - \mathbf{x}_0|_g$ has the expansion

$$|\mathbf{x} - \mathbf{x}_j|_g^2 = \varepsilon^2\rho_j^2 - \varepsilon^3\frac{\sin\theta_{1j}}{\xi_j}y_{1j}y_{2j}^2 + \mathcal{O}(\varepsilon^4)\,; \qquad \rho_j \equiv \sqrt{y_{1j}^2 + y_{2j}^2}\,, \tag{3.2}$$

while the leading order terms in the Laplace-Beltrami operator (1.2c) are given by

$$\Delta_g = \frac{1}{\varepsilon^2}\Delta_{\mathbf{y}_j} + \frac{1}{\varepsilon}\frac{\sin\theta_{1j}}{\xi_j}\left(2y_1\partial_{y_{2j}}^2 - \partial_{y_{1j}}\right) + \mathcal{O}(1)\,, \tag{3.3}$$

where $\Delta_{\mathbf{y}} \equiv \partial_{y_1y_1} + \partial_{y_2y_2}$.

Seeking a leading order radially symmetric spot profile, we begin by letting $U_j \sim U_{j0}(\rho_j) + \varepsilon U_{j1}$ and $V_j \sim V_{j0}(\rho_j) + \varepsilon V_{j1}$, and substituting into (1.2). We then obtain the radially symmetric leading order core problem (upon dropping the subscripts on the ρ_j's),

$$\Delta_\rho U_{j0} - U_{j0}V_{j0}^2 = 0\,, \quad \Delta_\rho V_{j0} - V_{j0} + U_{j0}V_{j0}^2 = 0\,; \qquad \rho > 0 \tag{3.4a}$$

$$U_{j0}'(0) = V_{j0}'(0) = 0\,, \qquad U_{j0} \sim S_j\log\rho + \chi(S_j)\,, \quad V_{j0} \to 0 \ \text{ as } \ \rho \to \infty\,, \tag{3.4b}$$

where $\Delta_\rho \equiv \partial_{\rho\rho} + \rho^{-1}\partial_\rho$, and $\chi(S_j)$ is a nonlinear function of S_j that must be computed numerically. As expected, this leading order tangent plane approximation of (1.2) near $\mathbf{x} = \mathbf{x}_j$ leads to the same core problem first analyzed in [20]. For completeness, we show in Fig. 2 some typical profiles for U_{j0} and V_{j0}, along with the relationship $\chi(S)$.

Applying the divergence theorem to the first equation of (3.4a), and using the far-field condition of (3.4b), we obtain the relation

$$S_j = \int_0^\infty U_{j0}V_{j0}^2\rho d\rho\,, \tag{3.5}$$

where S_j is referred to as the spot strength of spot j. Because v is localized to an $\mathcal{O}(\varepsilon)$ extent near each of the discrete spot locations, in the outer region away from $\mathbf{x}_j$, and in the limit $\varepsilon \to 0$, the reaction term $\varepsilon^{-2}uv^2$ in (1.2a) can therefore be represented, in the sense of distributions, as a sum of weighted delta functions. With $\partial_t u \sim \mathcal{O}(\varepsilon^2)$ in the quasi-equilibrium state, the outer equation for u then becomes, to leading order

$$\Delta_g u + A = 2\pi\sum_{j=1}^N S_j\delta(\boldsymbol{\theta};\boldsymbol{\theta}_j)\,, \tag{3.6a}$$

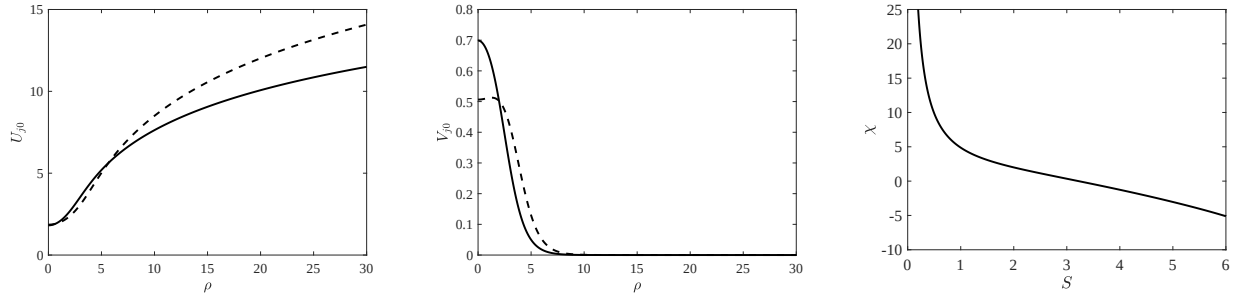

(a) $U_{j0}(\rho)$ (b) $V_{j0}(\rho)$ (c) $\chi(S)$

FIGURE 2. (a) and (b) Numerical solutions of (3.4) for $S \approx 3.92$ (solid) and $S \approx 5.07$ (dashed). As found in [20], the spot profile V_{j0} develops a volcano shape when $S \gtrsim 4.78$. (c) The relationship $\chi(S)$ defined in (3.4b).

with the matching condition

$$u \sim S_j \left[\log|\mathbf{x} - \mathbf{x}_j|_g + 1/\nu\right] + \chi(S_j) \;\text{ as }\; \boldsymbol{\theta} \to \boldsymbol{\theta}_j\,; \qquad \nu \equiv -\frac{1}{\log\varepsilon}\,. \tag{3.6b}$$

In (3.6b), we have used (3.2) to compute that $\log|\mathbf{x} - \mathbf{x}_j|_g \sim \log(\varepsilon\rho) + \mathcal{O}(\varepsilon)$.

The solvability condition for (3.6a) yields one equation for S_j,

$$\sum_{j=1}^{N} S_j = \frac{A|\Omega|}{2\pi}\,. \tag{3.7}$$

The solution for u can then be expressed in terms of the source-neutral Green's function as

$$u \sim -2\pi \sum_{j=1}^{N} S_j G_N(\boldsymbol{\theta}; \boldsymbol{\theta}_j) + \bar{u}\,, \tag{3.8}$$

where $\bar{u}$, the mean of u over Ω, is a constant to be found.

The final N equations for S_j and $\bar{v}$ come from matching the local behavior of (3.8) to that of (3.6b) near each spot location $\mathbf{x}_i$. To this end, we let $\mathbf{x} \to \mathbf{x}_i$ in (3.8) and match to the required local behavior of (3.6b) to obtain

$$S_i/\nu + 2\pi\left[S_i R_i + \sum_{j\neq i}^{N} S_j G_{ij}\right] + \chi_i = \bar{u}\,; \quad i = 1, \ldots, N\,. \tag{3.9}$$

where we have used (1.4) for the local behavior of $G_N(\boldsymbol{\theta}; \boldsymbol{\theta}_i)$ near $\boldsymbol{\theta}_i$. In (3.9), we have denoted $\chi_i \equiv \chi(S_i)$, $G_{ij} \equiv G_N(\boldsymbol{\theta}_i; \boldsymbol{\theta}_j)$, and $R_i \equiv R_N(\boldsymbol{\theta}_i; \boldsymbol{\theta}_i)$, where $R_N(\boldsymbol{\theta}; \boldsymbol{\theta}_i)$ is defined in (1.4). The nonlinear system of equations for S_j, $j = 1, \ldots, N$, along with $\bar{u}$ can be written compactly in matrix-vector form (see e.g., [20, 32]).

To shorten exposition and explicitly compare the theory to a numerical solution of (1.2), we consider the simple case of a single-spot pattern located at $\boldsymbol{\theta}_0$. In this case, (3.7) yields $S = A|\Omega|/(2\pi)$, while $\bar{u}$ is given by

$$\bar{u} = \frac{S}{\nu} + 2\pi S R_N(\boldsymbol{\theta}_0; \boldsymbol{\theta}_0) + \chi(S)\,. \tag{3.10}$$

Because $1/\nu$ is only logarithmically large in ε, the $\mathcal{O}(1)$ correction to $\bar{u}$ involving $R_N(\boldsymbol{\theta}_0; \boldsymbol{\theta}_0)$ is significant. Thus, in order to obtain an accurate outer approximation for u given by (3.8), we require an accurate solution for G_N not just away from $\boldsymbol{\theta}_0$, but also at $\boldsymbol{\theta}_0$.

In Fig. 3, we consider a solution of (1.2) consisting of one spot located at $\boldsymbol{\theta}_0 = (\pi, \pi)$, a true equilibrium location. In Fig. 3(a), we plot the activator component v, while the inhibitor component u is shown in Fig. 3(b). Blue (yellow) regions indicate small (large) values of the plotted variable. The solutions were obtained by solving (1.2) with $\partial_t u = \partial_t v = 0$ in FlexPDE7's finite element boundary value problem

solver [11]. In Figs. 3(c) and 3(d), we plot u along contours of constant θ_2 (3(c)) and θ_1 (3(d)), the contours of which are indicated in Fig. 3(b). The dashed lines are the exact solution as obtained from FlexPDE, while the solid is computed from (3.8) with $\bar{u}$ given in (3.10), and $R_N(\boldsymbol{\theta}_0;\boldsymbol{\theta}_0)$ computed using the analytic-numerical algorithm of §2. Even with $\varepsilon = 0.06$ only moderately small, we observe excellent agreement, the maximum error in both Figs. 3(c) and 3(d) both being approximately 0.19% (for $\varepsilon = 0.09$, we observe a maximum error of approximately 0.27%, confirming an increasing in error with ε). The agreement shows that $R_N(\boldsymbol{\theta}_0;\boldsymbol{\theta}_0)$ was indeed computed correctly.

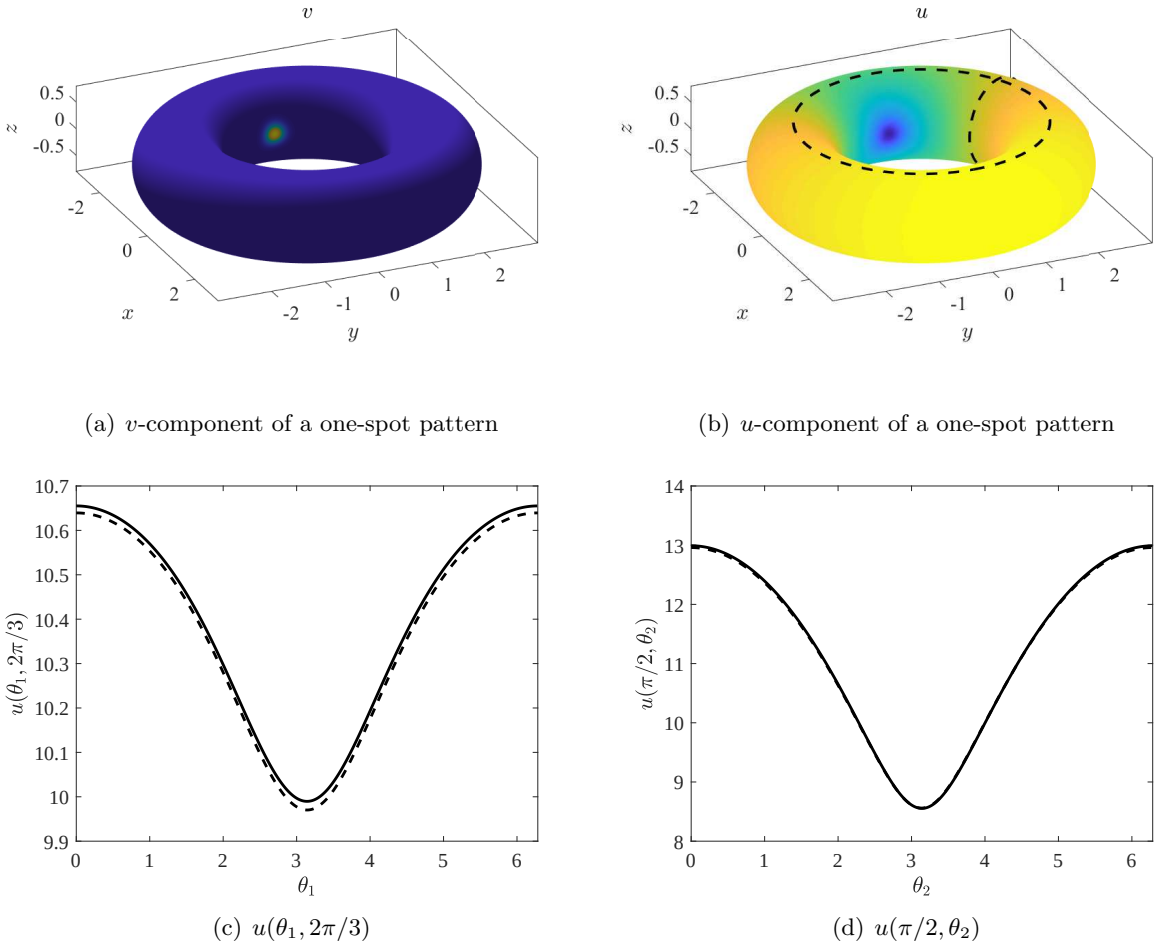

(a) v-component of a one-spot pattern

(b) u-component of a one-spot pattern

(c) $u(\theta_1, 2\pi/3)$

(d) $u(\pi/2, \theta_2)$

FIGURE 3. (a) and (b) Obtained through a finite elements solution of (1.2), the v- and u-components, respectively, of a one-spot pattern with $\varepsilon = 0.06$, $r = 0.8$, $R = 2.2$ and $A = 0.2635$. Blue (yellow) regions indicate small (large) values of the variable. (c) and (d) Comparison of u between the asymptotic solution (3.8) (solid) and that of the finite element solution (dashed). The maximum error in the two plots is approximately 0.19%. The particular contours on which the comparisons are made are indicated in (b).

We conclude this section by remarking that a quasi-equilibrium N-spot pattern may undergo a spot self-replication instability in which one or more spots may split into two. This occurs at the j-th spot when the spot strength S_j exceeds a certain threshold $\Sigma_2 \approx 4.3$, and may be triggered dynamically with slowly increasing A, r, and/or R. Because this instability is, to leading order, a local instability, the analysis and threshold for the torus are identical to that for the unit disk (see [20] for a detailed analysis and numerical simulations). We thus omit this from the discussion.

4. Slow drift dynamics

In this section, we analyze the slow drift dynamics of a one-spot pattern under the influence of the non-constant curvature of a torus. We show, numerically, that in the absence of repulsive interactions from other spots, a single spot will drift on the torus in the direction of decreasing curvature, and settle at a location of (locally) minimum curvature. As in other similar studies on flat 2D domains([20, 41, 6]) and the surface of the sphere ([39]), the drift speed is $\mathcal{O}(\varepsilon^2)$; the derived equation of motion below is valid in the absence of any instabilities that occur on an $\mathcal{O}(1)$ time-scale.

Instead of considering the general case of N spots, we will instead focus on the simple case of a single spot. The reasons are twofold. First, the analysis leading to a system of coupled differential algebraic equations for the locations and spot strengths of N spots on the torus is very similar to that for the sphere [39]. Second, the dynamics of a single spot highlight the effect of non-constant curvature on the drift dynamics. In particular, while a single spot remains stationary on the surface of a sphere, a spot on the torus will, in contrast, drift towards a location where the curvature has a local minimum. The main purpose of this section is to demonstrate the fact that the analytic-numerical method of §2 is able to yield a value for $\tilde{\nabla} R_N(\boldsymbol{\theta}_0;\boldsymbol{\theta}_0)$ that is sufficiently accurate to correctly predict the motion of a spot on a torus.

We begin by assuming that the center of the spot $\boldsymbol{\theta}_0 = (\theta_1^0, \theta_2^0)$ drifts slowly with a constant spot profile. That is, in the inner region, we let

$$y_1 = \frac{r(\theta_1 - \theta_1^0(\sigma))}{\varepsilon}\,, \quad y_2 = \frac{\xi_0(\theta_2 - \theta_2^0(\sigma))}{\varepsilon}\,; \qquad \mathbf{y} \equiv (y_1, y_2)\,, \tag{4.1}$$

where $\xi_0 \equiv R + r\cos\theta_1^0$, and $\sigma = \varepsilon^2 t$ is slow time. We also let $u \sim U_0(\rho) + \varepsilon U_1$, $v \sim V_0(\rho) + \varepsilon V_1$, and compute

$$\partial_t V_0 = -\varepsilon V_{0\rho}\mathbf{e}_\omega \cdot \boldsymbol{\gamma}_1\,; \qquad \boldsymbol{\gamma}_1 \equiv \begin{pmatrix} r\dot{\theta}_1^0 \\ \xi_0\dot{\theta}_2^0 \end{pmatrix}\,, \quad \mathbf{e}_\omega \equiv \begin{pmatrix} \cos\omega \\ \sin\omega \end{pmatrix}\,; \quad \mathbf{y} = \rho\mathbf{e}_\omega\,. \tag{4.2}$$

At the next order, using the expansion for the Laplace-Beltrami operator (3.3), we have for $\mathbf{W} \equiv (V_1, U_1)^T$,

$$\Delta_{\mathbf{y}}\mathbf{W} + \mathcal{M}\mathbf{W} = \mathbf{f}^c + \mathbf{f}^d\,; \qquad \mathcal{M} \equiv \begin{pmatrix} -1 + 2U_0V_0 & V_0^2 \\ -2U_0V_0 & -V_0^2 \end{pmatrix}\,, \tag{4.3a}$$

$$\mathbf{f}^c \equiv \frac{\sin\theta_1^0}{\xi_0}\left(\partial_{y_1} - 2y_1\partial_{y_2}^2\right)\begin{pmatrix} V_0 \\ U_0 \end{pmatrix}\,, \quad \mathbf{f}^d \equiv \begin{pmatrix} -V_{0\rho}\mathbf{e}_\omega\cdot\boldsymbol{\gamma}_1 \\ 0 \end{pmatrix}\,, \tag{4.3b}$$

where $\mathbf{f}^c$ arises due to the tangent plane approximation at $\boldsymbol{\theta} = \boldsymbol{\theta}_0$. The far-field behavior is obtained from the local behavior of u near $\boldsymbol{\theta} = \boldsymbol{\theta}_0$. We thus use (3.2) to expand (1.4) to the next order:

$$G_N \sim -\frac{1}{2\pi}\left[\log\rho + \log\varepsilon - \varepsilon\frac{\sin\theta_1^0}{2\xi_0\rho^2}y_1y_2^2\right] + R_N(\boldsymbol{\theta}_0;\boldsymbol{\theta}_0) + \varepsilon\tilde{\nabla}_0 R_N(\boldsymbol{\theta}_0;\boldsymbol{\theta}_0)\cdot\mathbf{y}\,, \tag{4.4}$$

where the operator $\tilde{\nabla}_0$ is defined in (1.5). With $u \sim -2\pi S G_N(\boldsymbol{\theta};\boldsymbol{\theta}_0) + \bar{u}$, the far-field behavior of $\mathbf{W}$ must then be

$$\mathbf{W} \sim \begin{pmatrix} 0 \\ -S\frac{\sin\theta_1^0}{2\xi_0\rho^2}y_1y_2^2 + \boldsymbol{\alpha}\cdot\mathbf{y} \end{pmatrix}\,, \tag{4.5a}$$

where

$$\boldsymbol{\alpha} \equiv -2\pi\tilde{\nabla}_0 R_N(\boldsymbol{\theta}_0;\boldsymbol{\theta}_0)\,. \tag{4.5b}$$

Following [39], we decompose $\mathbf{W}$ into a sum of a component $\mathbf{W}^c$ owing to curvature, along with a dynamic component $\mathbf{W}^d$, where $\mathbf{W}^c$ satisfies

$$\Delta_{\mathbf{y}}\mathbf{W}^c + \mathcal{M}\mathbf{W}^c = \mathbf{f}^c\,, \tag{4.6a}$$

$$\mathbf{W}^c \sim \begin{pmatrix} 0 \\ -S\frac{\sin\theta_1^0}{2\xi_0\rho^2}y_1y_2^2 \end{pmatrix} \text{ as } \rho\to\infty\,, \tag{4.6b}$$

with $\mathbf{f}^c$ defined in (4.3b). By Lemma 2 of [39], the solution to (4.6b) is

$$\mathbf{W}^c = \frac{y_2^2}{2}\frac{\sin\theta_1^0}{\xi_0}\partial_{y_1}\mathbf{W}_0 - \frac{\sin\theta_1^0}{\xi_0}y_1y_2\partial_{y_2}\mathbf{W}_0\,; \qquad \mathbf{W}_0 \equiv \begin{pmatrix} V_0 \\ U_0 \end{pmatrix}. \tag{4.7}$$

The dynamic component must therefore satisfy

$$\Delta_{\mathbf{y}}\mathbf{W}^d + \mathcal{M}\mathbf{W}^d = \mathbf{f}^d\,, \tag{4.8a}$$

$$\mathbf{W}^d \sim \begin{pmatrix} 0 \\ \boldsymbol{\alpha}\cdot\mathbf{y} \end{pmatrix} \text{ as } \rho\to\infty\,. \tag{4.8b}$$

With $\mathbf{f}^d$ defined in (4.3b), (4.8) is identical in form to (2.12) of [20]. Noting that there are two homogeneous solutions to (4.8), namely $\partial_{y_1}\mathbf{W}_0$ and $\partial_{y_2}\mathbf{W}_0$, we consider the adjoint problem

$$\Delta_{\mathbf{y}}\boldsymbol{\Psi} + \mathcal{M}^T\boldsymbol{\Psi} = \mathbf{0}\,, \qquad \boldsymbol{\Psi} \sim \begin{pmatrix} 0 \\ T(\omega)/\rho \end{pmatrix} \text{ as } \rho\to\infty\,, \tag{4.9}$$

where $T(\omega) \equiv \{\cos\omega, \sin\omega\}$. Multiplying (4.8a) by $\boldsymbol{\Psi}^T$ and integrating over a ball of radius R_B and letting $R_B\to\infty$, we appeal to Principal Result 2.1 of [20] to obtain that dynamics of the center of the spot $\boldsymbol{\theta}_0$ satisfies

$$\begin{pmatrix} r & 0 \\ 0 & \xi_0 \end{pmatrix}\dot{\boldsymbol{\theta}}_0 = \gamma(S)\boldsymbol{\alpha}\,; \qquad \gamma(S) \equiv \frac{-2}{\int_0^\infty V_{0\rho}P_1(\rho)\rho\,d\rho}\,, \tag{4.10}$$

where $\boldsymbol{\Psi}(\mathbf{y}) = \mathbf{P}(\rho)T(\omega)$, and $\mathbf{P}(\rho) \equiv (P_1(\rho), P_2(\rho))^T$. In (4.10), $\boldsymbol{\alpha}$ is given by (4.5b) in terms of the gradient of the regular part of $G_N(\boldsymbol{\theta};\theta_0)$ at $\boldsymbol{\theta} = \boldsymbol{\theta}_0$. The function $\gamma(S)$ must be computed numerically, and, for completeness, is shown in Fig. 4(a) (c.f. Fig. (3a) of [20]). By symmetry, the dynamics of a one-spot pattern are independent of θ_2^0, which remains constant in time.

In Fig. 4(b), we show the start and end locations of a one-spot quasi-equilibrium, as computed from a full finite elements solution of (1.2). The spot drifts toward an equilibrium location on the inner equator where the scalar curvature is minimum. In Fig. 4(c), we plot the time-evolution of the θ_1^0 component of the center of the spot as the spot drifts from the top of the torus ($\theta_1^0 = \pi/2$) to the inner equator ($\theta_1^0 = \pi$); the solid line is obtained from the full solution of (1.2), while the open circles are obtained from (4.10). The excellent agreement between the asymptotic prediction and numerical result (the maximum error with $\varepsilon = 0.06$ is approximately 1.6% and with $\varepsilon = 0.09$ is approximately 2.3%) indicates that the analytic-numerical method of §2 is accurate enough to yield not just the *value* of the regular part of G_N at the singular point, but also the value of the *gradient* of the regular part at the singular point. We remark that the outer equator of the torus (where the scalar curvature is maximum) is an unstable equilibrium. For the same parameter values as in Fig. 4, a spot initialized on the outer equator subject to a small perturbation would drift toward the inner equator via either the top or the bottom of the torus, depending on the nature of the perturbations.

In Figs. 4(d) and 4(e), we plot cross-sections in the θ_1 direction of the quantity $G_N(\boldsymbol{\theta};\boldsymbol{\theta}_0)+\chi(x(\boldsymbol{\theta}))\frac{1}{2\pi}\log|Tx(\boldsymbol{\theta})|$ through the singularity location $\boldsymbol{\theta}_0$ when $\theta_1^0 = \pi/2$ and $\theta_1^0 = \pi$, respectively, where χ is the smooth cutoff function defined in §2, and x is the normal coordinates defined in (2.2). The slope (dashed lines) of the function at the point $\boldsymbol{\theta}_0$ is what is used to compute $\nabla_0 R_N(\boldsymbol{\theta}_0;\boldsymbol{\theta}_0)$ in (4.5b). The slope is non-zero when $\theta_1^0 = \pi/2$, causing spot drift, and is equal to zero when $\theta_1^0 = \pi$, resulting in an equilibrium location. We emphasize that the sharp features are purely a result of subtracting off from G_N a multiple of the cutoff function χ; they do not affect the calculation of the slope at $\boldsymbol{\theta}_0$. These figures show that when we remove the logarithmic singularity from our numerically computed G_N, the resulting term is indeed smooth enough to be numerically differentiated and can be used to accurately predict spot motion. We have omitted corresponding plots of cross-sections in the θ_2 direction, as no spot drift occurs in that direction due to the symmetry of the torus. In Fig. 4(f), we plot the quantity $\partial_{\theta_1}R_N(\boldsymbol{\theta};\boldsymbol{\theta}_0)|_{\boldsymbol{\theta}=\boldsymbol{\theta}_0}$, the derivative of the regular part of R_N in the θ_1 direction, evaluated at the location of the singularity. We observe that it is equal to zero and is decreasing when $\theta_1 = 0$, leading to an unstable equilibrium on the outer equator, while it is equal to zero but is increasing when $\theta_1 = \pi$, leading to a stable equilibrium on inner equator.

We remark that the behavior of $\partial_{\theta_1} R_N(\boldsymbol{\theta};\boldsymbol{\theta}_0)|_{\boldsymbol{\theta}=\boldsymbol{\theta}_0}$ shown in Fig. 4(f) is qualitatively similar to the behavior of the gradient of the scalar curvature of the torus. However, the determination of an analytic relationship between the regular part $R_N(\boldsymbol{\theta};\boldsymbol{\theta}_0)$ with the curvature remains an open problem.

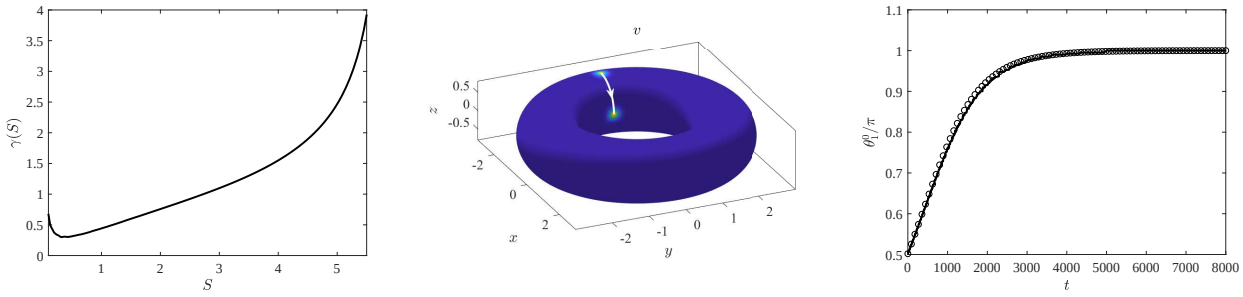

(a) $\gamma(S)$ (b) spot path (c) $\theta_1^0(t)$

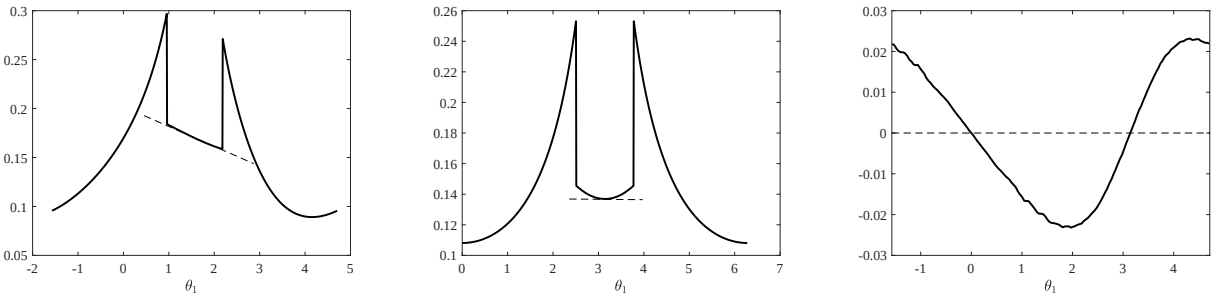

(d) cross section when $\theta_1^0 = \pi/2$ (e) cross section when $\theta_1^0 = \pi$ (f) $\partial_{\theta_1} R_N(\boldsymbol{\theta};\boldsymbol{\theta}_0)|_{\boldsymbol{\theta}=\boldsymbol{\theta}_0}$

FIGURE 4. (a) The quantity $\gamma(S)$ of (4.10). (b) The start and end locations of a one-spot quasi-equilibrium, as computed by a FlexPDE of (1.2). (c) The evolution of $\theta_1^0(t)$ from $\pi/2$ (top of the torus) to π (inner equator)— as obtained from a full solution of (1.2) (solid) and from the asymptotic prediction of (4.10) (open circles). The equilibrium location is on the inner equator where the curvature is minimum. The parameters are $\varepsilon = 0.06$, $r = 0.8$, $R = 2.2$, and $A = 0.15$. By symmetry, the results are independent of θ_2^0, which remains constant in time. (d) and (e) Cross-sections of the quantity $G_N(\boldsymbol{\theta};\boldsymbol{\theta}_0) + \chi(x(\boldsymbol{\theta}))\frac{1}{2\pi}\log|Tx(\boldsymbol{\theta})|$ through the singularity location $\boldsymbol{\theta}_0$ when $\theta_1^0 = \pi/2$ and $\theta_1^0 = \pi$, respectively, where χ is the smooth cutoff function defined in §2, and x is the normal coordinates defined in (2.2). The slope (dashed lines) of the function at the point $\boldsymbol{\theta}_0$ is what is used to compute $\nabla_0 R_N(\boldsymbol{\theta}_0;\boldsymbol{\theta}_0)$. The slope is non-zero when $\theta_1^0 = \pi/2$, causing spot drift, and zero when $\theta_1^0 = \pi$, resulting in an equilibrium location. Note that the sharp features are purely a result of subtracting off from G_n a multiple of the cutoff function χ; they do not affect the calculation of the slope at $\boldsymbol{\theta}_0$. (e) The slope of $R_N(\boldsymbol{\theta};\boldsymbol{\theta}_0)$ in the θ_1 direction at the location of the singularity. Note that it is equal to zero at the two equilibrium locations $\theta_1 = 0$ (the unstable outer equator) and $\theta_1 = \pi$ (the stable inner equator).

5. Oscillatory amplitude instabilities

In this section, we analyze the stability of a one-spot equilibrium (such as that of Fig. 3) to locally radially symmetric perturbations. We find that if the parameter τ in (1.2) exceeds a certain threshold τ_{H0}, the height of the spot undergoes oscillations of increasing amplitude at a certain frequency λ_{H0}. This occurs as a pair of complex eigenvalues crosses into the right half-plane through the imaginary axis at $\pm i\lambda_{H0}$ as τ is increased past τ_{H0}.

The analysis follows that of a one-spot equilibrium on the unit disk [47]. The main point of emphasis in this section will be the accuracy with which the methods of §2 are able to compute the Helmholtz

Green's function of (1.6), especially the value of its regular part at the singularity. That is, to obtain the threshold τ_{H0}, we require the value of $R_H(\boldsymbol{\theta}_0;\boldsymbol{\theta}_0)$, where the regular part $R_H(\boldsymbol{\theta};\boldsymbol{\theta}_0)$ is defined as

$$G_H(\boldsymbol{\theta};\boldsymbol{\theta}_0;k) \sim -\frac{1}{2\pi}\log|\boldsymbol{\theta}-\boldsymbol{\theta}_0|_g + R_H(\boldsymbol{\theta};\boldsymbol{\theta}_0;k) \text{ as } \boldsymbol{\theta}\to\boldsymbol{\theta}_0\,. \tag{5.1}$$

Since no analytic formula exists for $G_H(\boldsymbol{\theta};\boldsymbol{\theta}_0;k)$, an accurate numerical determination of $R_H(\boldsymbol{\theta}_0;\boldsymbol{\theta}_0)$ is essential for computing τ_{H0}.

We begin by linearizing around the equilibrium by letting $u = u_e(\boldsymbol{\theta}) + \psi(\boldsymbol{\theta})e^{\lambda t}$, $v = v_e(\boldsymbol{\theta}) + \phi(\boldsymbol{\theta})e^{\lambda t}$, to obtain the linearized eigenvalue problem

$$\lambda\phi = \varepsilon^2\Delta_g\phi - \phi + 2u_ev_e\phi + v_e^2\psi\,, \tag{5.2a}$$

$$\tau\lambda\psi = \Delta_g\psi - \frac{1}{\varepsilon^2}\left(2u_ev_e\phi + v_e^2\psi\right)\,. \tag{5.2b}$$

In the inner region, we let $\phi\sim\Phi(\mathbf{y})$ and $\psi\sim\Psi(\mathbf{y})$ to obtain from (5.2)

$$\lambda\Phi = \Delta_\rho\Phi - \Phi + 2U_0V_0\Phi + V_0^2\Psi\,, \tag{5.3a}$$

$$0 = \Delta_\rho\Psi - 2U_0V_0\Phi - V_0^2\Psi\,, \tag{5.3b}$$

with boundary and far-field conditions

$$\Phi'(0) = \Psi'(0) = 0\,,\quad \Phi\to 0\,,\quad \Psi\sim\log\rho + B(\lambda) \text{ as } \rho\to\infty\,. \tag{5.3c}$$

In (5.3a) and (5.3b), U_0 and V_0 are the solutions to the core problem (3.4). The coefficient of unity on the $\log|\mathbf{y}|$ term in (5.3c) acts as a normalization of the eigenfunctions. The normalization specifies $B(\lambda)$, which must be computed numerically. Applying the divergence theorem to (5.3b) and (5.3c), we find

$$\int_0^\infty (2U_0V_0\Phi + V_0^2\Psi)\rho d\rho = 1\,. \tag{5.4}$$

Consequently, in the outer region, the $\varepsilon^{-2}(2u_ev_e\phi + v_e^2\psi)$ term of (5.2b) may be replaced, in the sense of distributions, by a 2π-weighted delta function, resulting in

$$\Delta_g\psi - \tau\lambda\psi = 2\pi\delta(\boldsymbol{\theta};\boldsymbol{\theta}_0)\,. \tag{5.5}$$

Comparing (5.5) with (1.6), we identify $\psi = -2\pi G_H(\boldsymbol{\theta};\boldsymbol{\theta}_0;\lambda\tau)$ and $k=\tau\lambda$. Using (1.4), we thus have the local behavior for ψ near $\boldsymbol{\theta}_0$

$$\psi\sim\log\rho + \log\varepsilon - 2\pi R_H(\boldsymbol{\theta}_0;\boldsymbol{\theta}_0;\lambda\tau)\,. \tag{5.6}$$

Matching the constant terms in (5.6) to (5.3c), we obtain

$$B(\lambda) = \log\varepsilon - 2\pi R_H(\boldsymbol{\theta}_0;\boldsymbol{\theta}_0;\lambda\tau)\,. \tag{5.7}$$

Seeking a Hopf bifurcation, we let $\lambda = i\lambda_{H0}$ in (5.7) and equate real and imaginary parts, yielding a system of two equations for τ_{H0} and λ_{H0}.

In Fig. 5(a), we plot τ_{H0} versus r on the inner equator $\theta_0^1=\pi$ while holding the ratio rR constant at $rR=2$. Values of τ above the stability threshold lead to an unstable one-spot equilibrium, resulting in growing oscillations in the spot amplitude. In Figs. 5(b) and 5(c), we let $r=1$, $R=2$, and $A=0.1$ so that $S\approx 1.26$. Solving the system (5.7), we find $\tau_{H0}\approx 0.159$ and $\lambda_{H0}\approx 0.403$. In Fig. 5(b), we observe decaying amplitude oscillations when $\tau=0.15<\tau_{H0}$, while in Fig. 5(c), where $\tau=0.17>\tau_{H0}$, we observe growing amplitude oscillations. From the numerical results presented in both figures, we compute an angular frequency of approximately $\lambda_{H0}^{num}\approx 0.393$, in agreement with our asymptotic prediction.

In Fig. 5(a), τ_{H0} is a decreasing function of r over the range shown. This implies that a stable one-spot equilibrium on the inner equator may be dynamically destabilized by an increasing r while keeping $rR=2$ constant. With the scalar curvature at $\theta_1^0=\pi$ given by $S_s(r,R) = -2/(r(R-r))$, we observe that $S_s(r,2/r)<0$ and is a decreasing function of $r\in(0,\sqrt{1/2})$. Varying r and R in this way ensures that the surface area, and therefore, spot strength S, remains constant, and that the destabilization is due entirely to the decreasing scalar curvature at the location of the spot.

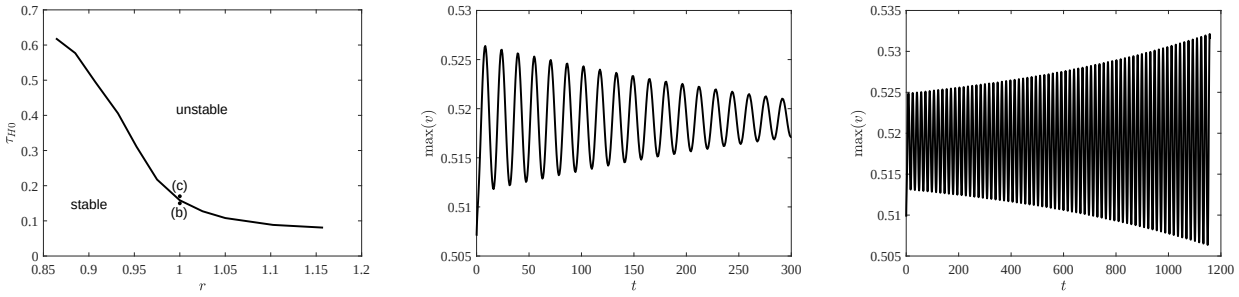

(a) τ_{H0} versus r (b) $r = 1$, $\tau = 0.15$ (c) $r = 1$, $\tau = 0.17$

FIGURE 5. (a) At $\theta_1^0 = \pi$, the Hopf instability threshold versus r for $rR = 2$ and $\varepsilon = 0.06$. The values of τ for (b) and (c) are indicated. (b) With $\varepsilon = 0.06$, $A = 0.1$, $r = 1$ and $R = 2$, the asymptotic prediction is $\tau_{H0} \approx 0.159$. Setting $\tau = 0.15 < \tau_{H0}$, spot amplitude undergoes decaying oscillations. (c) With $\tau = 0.17 > \tau_{H0}$, the single-spot pattern is unstable and the amplitude undergoes growing oscillations of angular frequency $\lambda_{H0}^{num} \approx 0.393$, which agrees well with our asymptotic prediction of $\lambda_{H0} \approx 0.403$.

In Fig. 6(a), we show the crossing of the Hopf bifurcation point as r is slowly increased past ≈ 0.9 while τ is held constant at 0.55. In Fig. 6(b), we show the amplitude of a spot on the inner equator resulting from solving (1.2) with $r = 0.8 + 0.001t$. When $r \lesssim 0.95$, the oscillation of the spot amplitude decays, indicating stability. However, as r is increased past 0.95, the oscillations begin to grow. The oscillations occur with angular frequency $\lambda_{H0}^{num} \approx 0.273$, which agrees well with the asymptotic prediction of $\lambda_{H0} \approx 0.27$. We observe a slight delayed bifurcation effect due to the initial decay of the perturbation; this effect was analyzed in detail in [43] for the case of 1-D localized patterns. In Figs. 6(c) and 6(d), we show two plots of v during the evolution, illustrating a scenario in which changing the geometry of the surface can affect the stability of the spot even with other parameters held constant. In Fig. 6(c), with $r = 0.8$ and scalar curvature $S_s \approx -1.47$, the spot is stable when $A = 0.1$. However, for the same value of A, the spot is unstable when $r = 1.1$ and $S_s \approx -2.53$.

The destabilizing effect of decreasing curvature when $r \approx 1$ suggests that a single spot, which from the results of §4, drifts in the direction of decreasing curvature, can *intrinsically* trigger a bifurcation by its drift. In Fig. 7, we illustrate this scenario by setting $\tau = 0.18$ and the initial spot location $\theta_1^0(0) = \pi - 0.35$. In Fig. 7(a), we plot τ_{H0} versus θ_1^0 for $r = 1$ and $S = 1.26$, showing indeed that the decreasing curvature as the spot nears the inner equator has a destabilizing effect. The arrow represents the slow drift of the spot from a stable region in parameter space to an unstable one as it approaches its equilibrium location on the inner equator. In Figure 7(b), we plot its location as a function of time, while in Figure 7(c), we plot its corresponding amplitude. We observe oscillations that initially decay, indicating stability. As the spot drifts toward the inner equator, oscillations begin to grow due to the destabilizing effect of decreasing curvature.

We remark that the analytic predictions for stability thresholds in the above cases of dynamically triggered instabilities relies on the separation of time-scales. That is, while the Hopf instability being triggered occurs on an $\mathcal{O}(1)$ time-scale, the triggering mechanisms themselves (i.e., the deformation of the torus, and the drift of the spot) evolve slowly in time. As such, the linear stability problem (5.2) remains time-independent to leading order. For more on the intrinsic triggering of $\mathcal{O}(1)$ instabilities by slow drift dynamics, see [20]. For general treatments of reaction-diffusion on surfaces that evolve in time, in particular the advection terms that arise as a result of surface deformation, see [45, 22].

6. Competition instabilities

In this section, we analyze the dynamic triggering of a monotonic competition instability of a two-spot quasi-equilibrium pattern. In past studies (1-, 2-, and 3-D), competition (or overcrowding) instabilities of N-spot patterns have typically been triggered in one of two ways. The first is through extrinsically

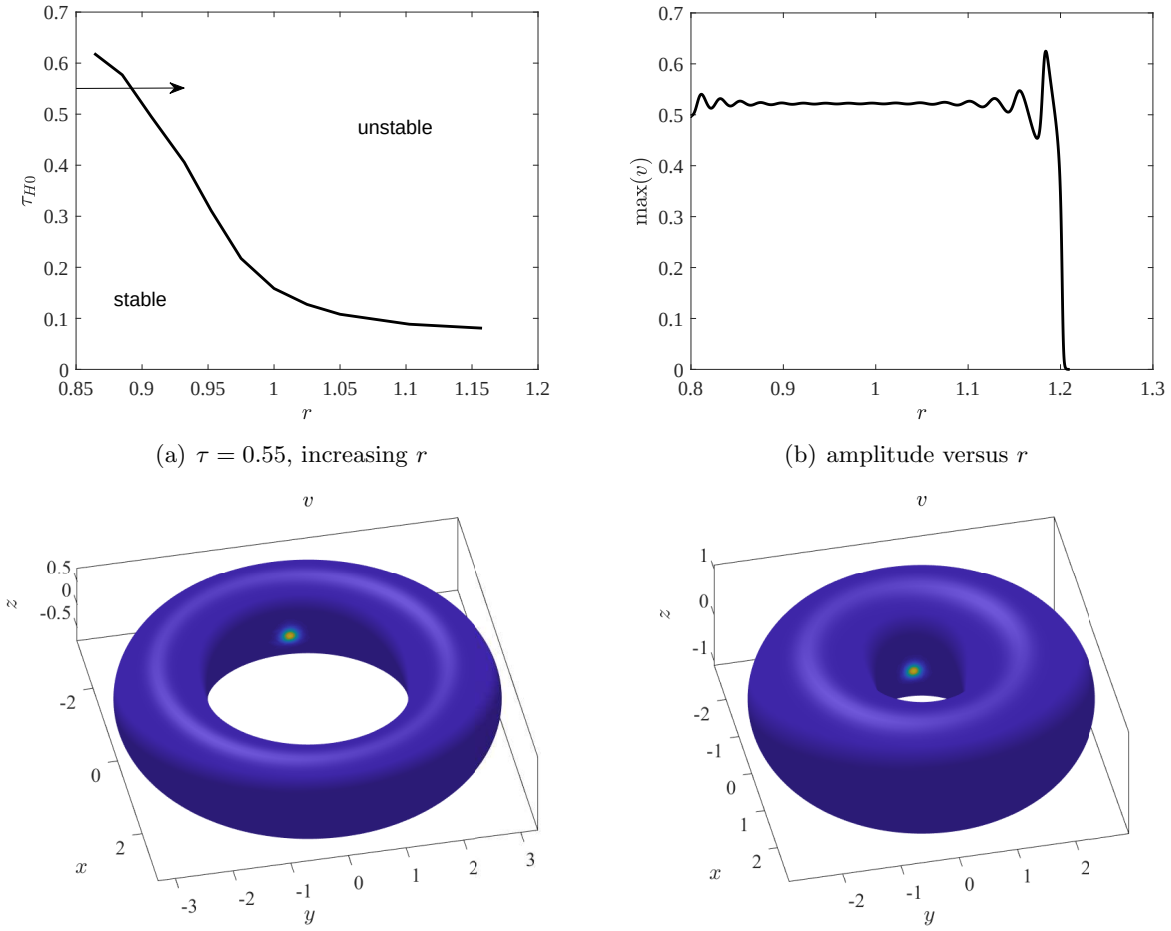

(a) $\tau = 0.55$, increasing r

(b) amplitude versus r

(c) $r = 0.8$; stable

(d) $r = 1.1$; unstable

FIGURE 6. (a) Schematic of the dynamically triggered bifurcation as r is increased past $r = 0.9$ while τ is held constant at $\tau = 0.55$. (b) Plot of the amplitude of the spot as r increases. An initially stable pattern (indicated by decaying oscillations when $r \lesssim 0.95$) becomes unstable as r is slowly increased. This results in growing amplitude oscillations of angular frequency $\lambda_{H0}^{num} \approx 0.273$, which compares favorably to the asymptotic prediction of $\lambda_{H0} \approx 0.27$. (c) and (d) Plot of v at two different times in the evolution. When $r = 0.8$, the spot is stable, while it is unstable when $r = 1.1$. The parameters are $r = 0.8 + 0.001t$, $R = 2/r$, $A = 0.1$, $\tau = 0.55$, and $\varepsilon = 0.06$.

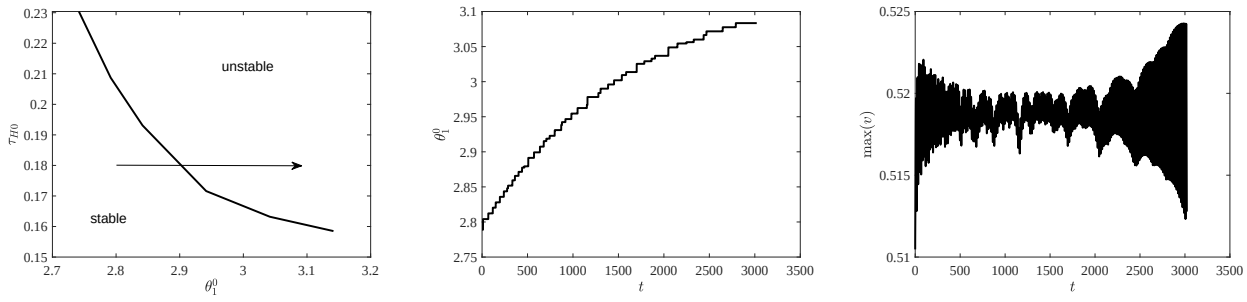

(a) τ_{H0} versus θ_1^0

(b) θ_1^0 versus t

(c) max(v) versus t

FIGURE 7. (a) The Hopf stability threshold τ_{H0} versus θ_1^0 for $r = 1$ and $S = 1.26$. The arrow represents the slow drift of the spot with $\tau = 0.18$. (b) and (c) Spot location and corresponding amplitude versus time. Initially decaying oscillations transition to growing oscillations as the drift into a region of decreasing curvature destabilizes the spot. Parameter values are $r = 1$, $R = 2$, $A = 0.1$, $\tau = 0.18$, and $\varepsilon = 0.06$.

decreasing the total feed-rate $A|\Omega|$ past a certain threshold, rendering the system incapable of supporting N-spots. The second is through the decrease of inter-spot distances via the intrinsic drift of the spots (e.g., two spots in 1-D drifting towards each other due to the repelling boundaries). In both cases, a single real eigenvalue crosses from the left-half to the right-half plane through the origin, and leads to a nonlinear annihilation of one or more of the spots. This latter example suggests that a competition instability can be triggered by a slow deformation of the torus that results in the decrease of the geodesic distance between two spots.

In this example, we extrinsically trigger the instability by slowly decreasing the minor radius r of the torus while keeping the quantities rR and A constant. We also place the spots at the equilibrium locations $\theta_{11} = \theta_{12} = \pi$ so that they remain stationary as the torus deforms. The dynamic triggering is thus driven solely by the changing geometry of the domain, and not by a decreasing total feed-rate (e.g., [42]) or intrinsic spot motion.

The stability analysis follows closely that of [5] (see §2.1) and [42] (see §3). For brevity, we omit the analysis, and directly quote the result. In particular, from (2.14) of [5], we obtain that the $\mathcal{O}(1)$ stability of an N-spot quasi-equilibrium solution of (1.2) is governed by the following globally coupled eigenvalue problem (GCEP):

$$\mathcal{M}(\lambda; r)\mathbf{c} = \mathbf{0}\,; \quad M(\lambda; r) \equiv \mathcal{I} + 2\pi\nu\mathcal{G}_\lambda + \nu\mathcal{B}\,; \tag{6.1a}$$

$$(\mathcal{G}_\lambda)_{ij} \equiv \begin{cases} R_H(\boldsymbol{\theta}_i; \boldsymbol{\theta}_i; \lambda\tau) & i = j \\ G_H(\boldsymbol{\theta}_i; \boldsymbol{\theta}_j; \lambda\tau) & i \neq j \end{cases}, \qquad (\mathcal{B})_{ij} \equiv \delta_{ij} B_i(\lambda)\,, \tag{6.1b}$$

where $\mathcal{I}$ is the $N \times N$ identity matrix, $\nu = -1/\log\varepsilon$, and $\mathbf{c}$ is an N-vector of coefficients determining the mode of instability. In our example where two spots are symmetrically placed on the inner equator, $\mathbf{c} = (1, 1)^T$ corresponds to the synchronous mode of instability, while $\mathbf{c} = (1, -1)^T$ corresponds to the asynchronous mode. As in past studies, the former is associated with a Hopf bifurcation resulting in synchronous oscillation of spot amplitudes, while the latter is associated with the monotonic competition instability.

In (6.1a), the dependence of $\mathcal{M}$ on r is via the interaction matrix $\mathcal{G}_\lambda$. In (6.1b), $B_j(\lambda)$ is obtained from (5.3) by replacing (U_0, V_0) by the local solution (U_{j0}, V_{j0}) of (3.4). In seeking the threshold criteria, we take the limit $\lambda \to 0$ in (6.1) so that G_H and R_H may be replaced by the source-neutral functions G_N and R_N defined in (1.3a) and (1.4). Further, when $\lambda = 0$ in (5.3), we differentiate (3.4) with respect to S_j to find that $B_j(0) = \partial_{S_j}\chi(S_j)$.

In Figure 8(a), we compute $\det\mathcal{M}(0)$ for a range of r, with the major axis given by $R = 2/r$ so that $rR = 2$. For $r \approx 1.06$, we observe that $\det\mathcal{M}(0) = 0$, with the null space of $\mathcal{M}(0)$ being spanned by $\mathbf{c} = (1, -1)$. As such, as r increases past $r = 1.06$, we expect a competition instability to be triggered, resulting in the annihilation of one of the spots. This is confirmed in Fig. 8(b), where we plot $\max(v)$ versus r. In the inset, we observe an exponential increase in the amplitude of one of the spots shortly after r is increased past $r \approx 1.06$, indicating the onset of the competition instability.

In Figs. 8(c) and 8(d), we show the two spots on the inner equator of a torus with minor radius $r = 0.8 + 0.001t$ and major radius $R = 2/r$. In Fig. 8(c), $r = 0.95$, leading to a stable two-spot pattern. In Fig. 8(d), we show the pattern when $r = 1.3$. The instability has set in, and one of the spots is in the midst of being annihilated, thus appearing lighter than the other.

7. Discussion

We have introduced an analytic-numerical framework for accurately computing, on a surface of varying curvature, properties of Green's functions at the location of the singularity. The main idea is that we are able to resolve the singularity expansion of the Green's function by integrating a series of transport equations in the appropriate coordinate system (normal coordinates). Once this is done, the remaining part of the Green's function can then be obtained by numerically solving an elliptic PDE with a regular non-homogenous term. The analytic construction of the singular terms and formulation of the smooth

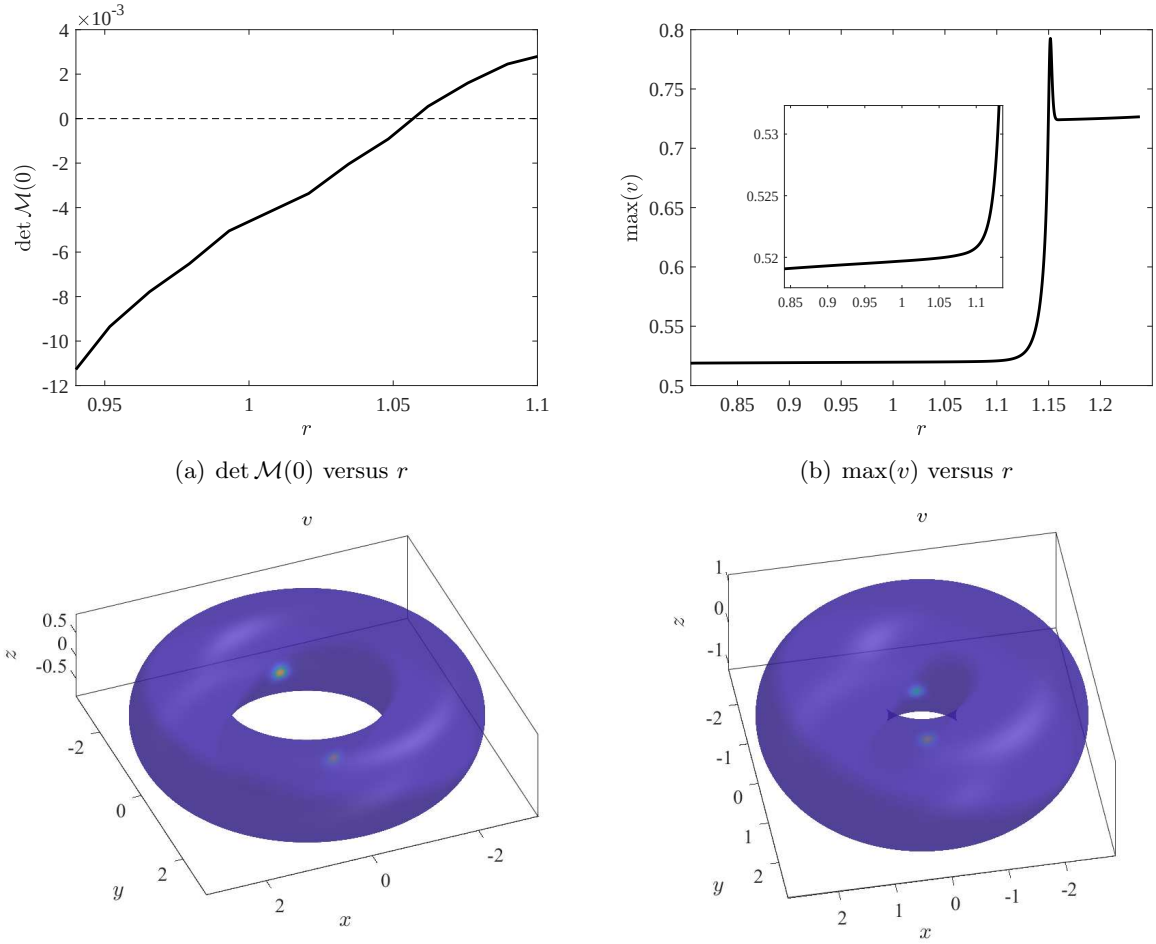

(a) $\det \mathcal{M}(0)$ versus r

(b) $\max(v)$ versus r

(c) $r = 0.9$; stable

(d) $r = 1.149$; unstable

FIGURE 8. (a) Plot of $\det \mathcal{M}(0)$ versus r with $N = 2$ spots symmetrically placed on the inner equator. The zero crossing at $r \approx 1.06$, with corresponding null space spanned by $\mathbf{c} = (1, -1)$, indicates the presence of a competition instability when $r > 1.06$. (b) Plot of $\max(v)$ versus r as r is slowly increased in time. Near $r \approx 1.06$, we observe an exponential increase in $\max(v)$, indicating the onset of a competition instability. (c) A two-spot equilibrium pattern on the torus with $r = 0.9$. (d) After onset, one of the spots undergoes a nonlinear annihilation, resulting in a one-spot pattern (not shown). The parameters are $r = 0.8 + 0.001t$, $R = 2/r$, $A = 0.2$, $\varepsilon = 0.06$, and $\tau = \varepsilon^2$.

numerical PDE together allow properties of the Green's function to be computed to a high degree of accuracy, even at the location of the singularity.

To demonstrate its effectiveness and accuracy, we coupled it with a hybrid asymptotic-numerical method to analyse localized spot patterns on the surface of a ring torus. By using the analytic-numerical framework to compute the values of the regular parts of the Helmholtz and source-neutral Green's functions at the locations of the singularity, we were able to obtain highly accurate predictions for oscillatory and monotonic amplitude instabilities, including those dynamically triggered, associated with a single- and two-spot pattern, respectively. In both of these cases, in the parameter regimes that we considered, we observed that decreasing Gaussian curvature appears to have a destabilizing effect on an equilibrium spot pattern.

By using the analytic-numerical method to accurately compute the *gradient* of the regular part of the source-neutral Green's function at the singularity, we accurately predicted the slow drift dynamics of a single spot. In particular, we showed that in contrast to case of the sphere [39], which has constant curvature, a single spot on a torus will drift toward the inner equator, where the Gaussian curvature is minimized. We emphasize, however, that a spot drifts according to the gradient of the regular part of

the source-neutral Green's function at the location of the singularity, and not according to the gradient of the Gaussian curvature. Determining an analytic relationship between these two quantities is an open problem. All asymptotic results were confirmed by full numerical solutions of the Schnakenberg PDE system. Work on the more difficult analysis of the slow oscillatory drift instability [47], which requires the *Hessian* of the Helmholtz Green's function, is currently in progress.

The utility of our analytic-numerical method is not limited to the special cases that we have considered here. While we considered only Green's functions on the torus satisfying $\Delta_g G_N - |\Omega|^{-1} = -\delta(\boldsymbol{\theta};\boldsymbol{\theta}_0)$ and $(\Delta_g - k)G_H = -\delta(\boldsymbol{\theta};\boldsymbol{\theta}_0)$, where k is a constant parameter, the theory is applicable to operators of the form $\Delta_g + X - V$ for any metric tensor g, first order operator X, and smooth potential V. As such, the analytic-numerical framework that we have introduced can be paired with the hybrid asymptotic-numerical method to analyse a variety of reaction-diffusion models on a variety of different types of surfaces. Of particular relevance for the modeling of vegetation patterns, for example, would be surfaces that are graphs with the parametrization $x = x, y = y, z = f(x, y)$ [1, 26, 28]. Surfaces of more theoretical interest may be those of genus two or higher. For such surfaces, the pair-of-pants decomposition [13] can be used to reduce the problem on a surface of any genus to a computation on finitely many copies of a disk with two holes cut out. The matching conditions on the boundaries are provided by the pair of pants decomposition framework.

Lastly, we note two other singular perturbation problems that our analytic-numerical framework would be effective at addressing. The first is the problem of optimizing the fundamental Neumann eigenvalue for the Laplacian in a domain with small Dirichlet traps [17, 7]. The other closely related problem is the so-called narrow escape or narrow capture problem [9, 8, 30, 35, 36, 37], which computes the mean first-passage time of a random particle to a set of small Dirichlet traps. Both are mixed boundary value problems that can be solved asymptotically in terms of Green's functions using the hybrid asymptotic-numerical method of [46]. In particular, the critical quantity required in the analysis is the value of the regular part of the source-neutral Green's function at the location of the singularity, the same quantity used in the computation of $\bar{u}$ in (3.10). Considering these types of problems on a curved surface becomes relevant in the modeling of, for example, diffusion of molecules on cell membranes (e.g., [4, 14] and references therein). While the narrow capture problem has been considered for the special case of the spherical surface [9], concrete results regarding how variable surface curvature impacts mean first-passage times still have not been obtained. The analytic-numerical method that we have introduced here, combined with a hybrid asymptotic-numerical method, would be an effective tool for opening this avenue of analysis.

Acknowledgments

The authors gratefully acknowledge the insightful contributions of Michael J. Ward (University of British Columbia) and Christopher Green (Macquarie University).

References

[1] J. E. Baartman, A. J. Temme, and P. M. Saco, *The effect of landform variation on vegetation patterning and related sediment dynamics*, Earth Surface Processes and Landforms, 43 (2018), pp. 2121–2135.

[2] R. Bastiaansen, P. Carter, and A. Doelman, *Stable planar vegetation stripe patterns on sloped terrain in dryland ecosystems*, arXiv preprint arXiv:1811.10226, (2018).

[3] R. Bastiaansen, M. Chirilus-Bruckner, and A. Doelman, *Pulse solutions for an extended Klausmeier model with spatially varying coefficients*, arXiv preprint arXiv:1812.07804, (2018).

[4] A. J. Borgdorff and D. Choquet, *Regulation of ampa receptor lateral movements*, Nature, 417 (2002), p. 649.

[5] Y. Chang, J. Tzou, M. Ward, and J. Wei, *Refined stability thresholds for localized spot patterns for the Brusselator model in* $\mathbb{R}^2$, Eur. J. Appl. Math, 26 (2017).

[6] W. Chen and M. J. Ward, *The stability and dynamics of localized spot patterns in the two-dimensional Gray–Scott model*, SIAM Journal on Applied Dynamical Systems, 10 (2011), pp. 582–666.

[7] A. Cheviakov and M. J. Ward, *Optimizing the principal eigenvalue of the Laplacian in a sphere with interior traps*, Math. and Comp. Modeling, 53 (2011), pp. 1394–1409.

[8] A. F. Cheviakov, M. J. Ward, and R. Straube, *An asymptotic analysis of the mean first passage time for narrow escape problems: Part II: The sphere*, SIAM Multiscale Modeling & Simulation, 8 (2010), pp. 836–870.

[9] D. Coombs, R. Straube, and M. Ward, *Diffusion on a sphere with localized traps: Mean first passage time, eigenvalue asymptotics, and Fekete points*, SIAM Journal on Applied Mathematics, 70 (2009), pp. 302–332.
[10] A. Doelman, R. A. Gardner, and T. J. Kaper, *Stability analysis of singular patterns in the 1d Gray-Scott model: a matched asymptotics approach*, Physica D: Nonlinear Phenomena, 122 (1998), pp. 1–36.
[11] FlexPDE7, PDE Solutions Inc. URL http://www.pdesolutions.com, (2017).
[12] C. C. Green and J. S. Marshall, *Green's function for the Laplace–Beltrami operator on a toroidal surface*, Proc. R. Soc. A, 469 (2013), p. 20120479.
[13] A. Hatcher and W. Thurston, *A presentation for the mapping class group of a closed orientable surface*, Topology, 19 (1980), pp. 221–237.
[14] D. Holcman and Z. Schuss, *Escape through a small opening: receptor trafficking in a synaptic membrane*, Journal of Statistical Physics, 117 (2004), pp. 975–1014.
[15] L. Hörmander, *Analysis of Linear Partial Differential Operators*, vol. 3, Springer-Verlag, New York, 1989.
[16] D. Iron, M. J. Ward, and J. Wei, *The stability of spike solutions to the one-dimensional Gierer–Meinhardt model*, Physica D: Nonlinear Phenomena, 150 (2001), pp. 25–62.
[17] T. Kolokolnikov, M. S. Titcombe, and M. J. Ward, *Optimizing the fundamental Neumann eigenvalue for the Laplacian in a domain with small traps*, Europ. J. Appl. Math., 16 (2005), pp. 161–200.
[18] T. Kolokolnikov, M. Ward, J. Tzou, and J. Wei, *Stabilizing a homoclinic stripe*, Philosophical Transactions of the Royal Society A: Mathematical, Physical and Engineering Sciences, 376 (2018), p. 20180110.
[19] T. Kolokolnikov, M. J. Ward, and J. Wei, *The existence and stability of spike equilibria in the one-dimensional Gray–Scott model: The pulse-splitting regime*, Physica D: Nonlinear Phenomena, 202 (2005), pp. 258–293.
[20] T. Kolokolnikov, M. J. Ward, and J. Wei, *Spot self-replication and dynamics for the Schnakenberg model in a two-dimensional domain*, J. Nonlinear Sci., 19 (2009), pp. 1–56.
[21] T. Kolokolnikov and J. Wei, *Pattern formation in a reaction-diffusion system with space-dependent feed rate*, SIAM Review, 60 (2018), pp. 626–645.
[22] A. L. Krause, M. A. Ellis, and R. A. Van Gorder, *Influence of curvature, growth, and anisotropy on the evolution of turing patterns on growing manifolds*, Bulletin of mathematical biology, 81 (2019), pp. 759–799.
[23] J. M. Lee, *Riemannian manifolds: an introduction to curvature*, vol. 176, Springer Science & Business Media, 2006.
[24] A. E. Lindsay, R. T. Spoonmore, and J. C. Tzou, *Hybrid asymptotic-numerical approach for estimating first-passage-time densities of the two-dimensional narrow capture problem*, Physical Review E, 94 (2016), p. 042418.
[25] P. Matthews, *Pattern formation on a sphere*, Physical Review E, 67 (2003), p. 036206.
[26] G. S. McGrath, K. Paik, and C. Hinz, *Microtopography alters self-organized vegetation patterns in water-limited ecosystems*, Journal of Geophysical Research: Biogeosciences, 117 (2012).
[27] J. E. Pearson, *Complex patterns in a simple system*, Science, 261 (1993), pp. 189–192.
[28] G. G. Penny, K. E. Daniels, and S. E. Thompson, *Local properties of patterned vegetation: quantifying endogenous and exogenous effects*, Philosophical Transactions of the Royal Society A: Mathematical, Physical and Engineering Sciences, 371 (2013), p. 20120359.
[29] P. Petersen, S. Axler, and K. Ribet, *Riemannian geometry*, vol. 171, Springer, 2006.
[30] S. Pillay, M. J. Ward, A. Peirce, and T. Kolokolnikov, *An asymptotic analysis of the mean first passage time for narrow escape problems: Part I: Two-dimensional domains*, Multiscale Modeling & Simulation, 8 (2010), pp. 803–835.
[31] W. N. Reynolds, S. Ponce-Dawson, and J. E. Pearson, *Self-replicating spots in reaction-diffusion systems*, Physical Review E, 56 (1997), p. 185.
[32] I. Rozada, S. J. Ruuth, and M. J. Ward, *The stability of localized spot patterns for the Brusselator on the sphere*, SIAM J. Appl. Dyn. Sys., 13 (2014), pp. 564–627.
[33] L. Sewalt and A. Doelman, *Spatially periodic multipulse patterns in a generalized Klausmeier–Gray–Scott model*, SIAM Journal on Applied Dynamical Systems, 16 (2017), pp. 1113–1163.
[34] E. Siero, A. Doelman, M. Eppinga, J. D. Rademacher, M. Rietkerk, and K. Siteur, *Striped pattern selection by advective reaction-diffusion systems: Resilience of banded vegetation on slopes*, Chaos: An Interdisciplinary Journal of Nonlinear Science, 25 (2015), p. 036411.
[35] A. Singer, Z. Schuss, and D. Holcman, *Narrow escape, Part II: The circular disk*, Journal of statistical physics, 122 (2006), pp. 465–489.
[36] A. Singer, Z. Schuss, and D. Holcman, *Narrow escape, Part III: Non-smooth domains and Riemann surfaces*, Journal of statistical physics, 122 (2006), pp. 491–509.
[37] A. Singer, Z. Schuss, D. Holcman, and R. Eisenberg, *Narrow escape, Part I*, Journal of Statistical Physics, 122 (2006), pp. 437–463.
[38] J. Smith-Roberge, D. Iron, and T. Kolokolnikov, *Pattern formation in bacterial colonies with density-dependent diffusion*, European Journal of Applied Mathematics, (2018), pp. 1–23.
[39] P. H. Trinh and M. J. Ward, *The dynamics of localized spot patterns for reaction-diffusion systems on the sphere*, Nonlinearity, 29 (2016), pp. 766–806.
[40] W. H. Tse, J. Wei, and M. Winter, *The Gierer–Meinhardt system on a compact two-dimensional Riemannian manifold: Interaction of Gaussian curvature and Green's function*, Journal de mathématiques pures et appliquées, 94 (2010), pp. 366–397.
[41] J. Tzou and M. Ward, *The stability and slow dynamics of spot patterns in the 2D Brusselator model: The effect of open systems and heterogeneities*, Physica D: Nonlinear Phenomena, 373 (2018), pp. 13–37.
[42] J. Tzou, S. Xie, T. Kolokolnikov, and M. J. Ward, *The stability and slow dynamics of localized spot patterns for the 3-D Schnakenberg reaction-diffusion model*, SIAM Journal on Applied Dynamical Systems, 16 (2017), pp. 294–336.

[43] J. C. Tzou, M. J. Ward, and T. Kolokolnikov, *Slowly varying control parameters, delayed bifurcations, and the stability of spikes in reaction–diffusion systems*, Physica D: Nonlinear Phenomena, 290 (2015), pp. 24–43.
[44] H. Uecker, *Pattern formation with pde2path–a tutorial*, arXiv preprint arXiv:1908.05211, (2019).
[45] R. A. Van Gorder, V. Klika, and A. L. Krause, *Non-autonomous turing conditions for reaction-diffusion systems on evolving domains*, arXiv preprint arXiv:1904.09683, (2019).
[46] M. J. Ward, W. D. Henshaw, and J. B. Keller, *Summing logarithmic expansions for singularly perturbed eigenvalue problems*, SIAM Journal on Applied Mathematics, 53 (1993), pp. 799–828.
[47] S. Xie and T. Kolokolnikov, *Moving and jumping spot in a two-dimensional reaction–diffusion model*, Nonlinearity, 30 (2017), p. 1536.